



A Data-Driven Search For Mid-Infrared Excesses Among Five Million Main-Sequence FGK Stars

GABRIELLA CONTARDO ¹ AND DAVID W. HOGG ^{2,3,4}

¹*Theoretical and Scientific Data Science, Scuola Internazionale Superiore di Studi Avanzati (SISSA), Trieste, Italy*

²*Center for Cosmology and Particle Physics, Department of Physics, New York University, New York NY, USA*

³*Center for Computational Astrophysics, Flatiron Institute, New York NY, USA*

⁴*Max-Planck-Institut für Astronomie, Heidelberg, Germany*

ABSTRACT

Stellar infrared excesses can indicate various phenomena of interest, from protoplanetary disks to debris disks, or (more speculatively) techno-signatures along the lines of Dyson spheres. In this paper, we conduct a large search for such excesses, designed as a data-driven contextual anomaly detection pipeline. We focus our search on FGK stars close to the main sequence to favour non-young host stars. We look for excess in the mid-infrared, unlocking a large sample to search in while favouring extreme IR excess akin to the ones produced by Extreme Debris Disks (EDD). We combine observations from ESA *Gaia* DR3, *2MASS*, and the *unWISE* version of NASA *WISE*, and create a catalogue of 4,898,812 stars with $G < 16$ mag. We consider a star to have an excess if it is substantially brighter in $W1$ and $W2$ bands than what is predicted from an ensemble of machine-learning models trained on the data, taking optical and near-infrared information as input features. We apply a set of additional cuts (derived from the ML models and the objects' astronomical features) to avoid false-positive and identify a set of 53 objects (a rate of 1.1×10^{-5}), including one previously identified EDD candidate. Typical infrared-excess fractional luminosities we find are in the range 0.005 to 0.1, consistent with known EDDs.

1. INTRODUCTION

The presence of infrared excess in stellar objects is, in general, a sign of circumstellar dust, protoplanetary disks, or debris disks. As such, they are often associated with (relatively) young stellar objects. The strength of IR excesses is expected to decrease as a function of stellar age as a star's disk evolves (Wyatt et al. 2015), tying it to the evolutionary process in the star, its potential planets and other planetesimals or asteroid belts. For instance, Cotten & Song (2016) detect IR excess in main-sequence stars, with a range of fractional luminosity between 10^{-5} to 10^{-2} , averaging around 10^{-4} , and with a single candidate having a $L_{IR}/L_* \simeq 0.1$. However, several studies have also highlighted the existence of high IR excess (with fractional luminosities around 0.02 and up to 0.1) for stellar objects aged between 10 and 200 Myr, and one older than 1 Gyr

(Moór et al. 2021; Balog et al. 2009). These fractional luminosities are in between the ones expected for (regular) debris disks ($L_{IR}/L_* < 10^{-3}$) and protostars ($L_{IR}/L_* > 0.1$) (Uzpen et al. 2005). Those excesses are currently thought to be associated with Extreme Debris Disks (EDD) created potentially after planetary collisions. However, the stellar ages of these candidates are in tension with the current models of rocky planet formation which predict that most collision events (leading to such disks) should occur within the first 100 Myr. Therefore, these objects might indicate that these processes last longer than thought or that other processes lead to such disks.

Currently, there are very few known EDD candidates: there were 17 reported in Moór et al. (2021), and those events are relatively rare: Moór et al. (2021) searched through 78,650 objects and found 8 candidates –6 new

and 2 known, i.e. an “occurrence”¹ rate of 0.01%. Hence, those extreme excesses come from rare or potentially very short-lived events. It is critical to increase our sample of candidates for statistics and follow-up investigations that will investigate the underlying physical causes of these extreme IR excesses and improve our understanding of planet formation.

Interestingly, another possible—albeit less likely—causes of extreme IR excess are techno-signatures such as Dyson Spheres (hypothetical megastructures built around stars to collect energy). For instance, Suazo et al. (2022) provided upper limits on the prevalence of partial Dyson Spheres combining data from *Gaia* DR2 and *AllWISE*, using models of the resulting IR-excess (and optical obscuration) of different types (stages and temperature) of Dyson Spheres. The search for (extreme) contextual outliers in the IR is a nice example where the search for extraterrestrial intelligence (SETI) field intersects and can challenge the boundaries of current astrophysical models (in this instance, of planetary formation and evolution). As one would need to investigate and eliminate all other explanations before concluding an extreme IR-excess source is a Dyson Sphere, searches for “Dysonian” signatures will potentially provide interesting objects for “mainstream” astrophysics. This aspect has been coined as the “ancillary benefit”, one of the axes of merits one can evaluate technosignature searches by, defined by Sheikh (2020).

We propose here to conduct a large search for extreme infrared excesses. We focus on a population of photometrically main-sequence stars, to favor potentially non-young or transitional candidates. We also restrict our search to FGK stars, to focus on Sun-like systems. We choose to conduct our search in the mid-IR, and more specifically we look for excess in the *WISE* *W1* and *W2* bands: It has been shown that IR-excess typical of EDDs are hot enough to show in *W1* and *W2*, and we expect (possibly extremely naively) to see techno-signatures near the water triple-point. Restricting to these two *WISE* bands unlocks a large sample, as the sensitivity and reliability of *WISE* is much higher in those bands than in the *W3* and *W4* bands. On the other hand, this means that we target only extreme events that can nonetheless be subtle (especially in the *W1* band).

¹ We note that due to the way the searches (including this one) are done—usually involving a variety of threshold-based or hard cuts, it is difficult to define properly the occurrence rate of those excesses.

To approach this problem in a way that scales to our curated catalogue of 4.9 million stars, we present a data-driven pipeline. Our approach alleviates the need for good stellar modelling or fitting: we are looking instead for deviations (or contextual anomalies) *according to the data*, i.e., our sample of main-sequence FGK stars. We train a machine learning model to predict the expected *W1* and *W2* magnitudes from other (optical and near-infrared) photometric features. We then look for stars that are confidently incorrectly predicted fainter than observed. This approach is also computationally interesting compared to “proper” SED fitting to scale to our 4.9 million objects dataset.

From a more general and methodological perspective, this paper presents a pipeline to conduct targeted, contextual anomaly detection (see Chandola et al. (2009) for an anomaly-detection taxonomy overview), benefiting from robust supervised machine learning methods (here Random Forest). Anomaly detection (in astronomy and astrophysics) is often framed as finding rare objects, i.e., finding data examples with low probability (in low-density regions) according to the data. To tackle this problem with ML methods, one can (for instance) get a density estimate, and retrieve the objects with low scores. Some caveats of this generic approach are that (i) obtaining reliable density estimates is non-trivial, especially as the number of dimensions increases, and (ii) such an approach will retrieve all (potentially) rare/odd objects, but not necessarily the “interesting ones” (which motivates the growing literature on integrating active-learning in anomaly detection pipeline in astronomy such as in Ishida et al. (2021) and Lochner & Bassett (2021)). However, it is a good way to potentially uncover the infamous “unknown unknowns”. On the other hand, in many cases, we might be looking for “known unknowns” (as in well-specified unknowns, like here, where we want to look for specific types of anomalies: stars with IR-excess). “Knowing” our unknowns, however, does not necessarily mean that we can turn this problem into a supervised classification one (where our detector would tell us a binary answer or a score probability of our object being an anomaly): We might not have actual examples of these anomalies, or only very few examples.

Here we propose to benefit from the fact that we are looking for targeted anomalies that deviate in a specific way (excess), in a specific region of the feature space (mid-infrared), considering their “context” (their optical and near-IR observations). We will be looking for objects that are confidently wrong in the prediction of that part of the feature space (the MIR-bands) using

the rest of the feature space (mostly optical and near-IR photometry, see Section 3 for details). This process is indirectly doing a form of density estimation: as we assume our model is flexible enough and generalizes well, objects with a high, confident error, deviate from the training set distribution in some significant ways, that are not predictable from their “context” (input features). We note however that if the objects we are looking for were very common in our sample and with an excess predictable from the input features, our pipeline would not flag them as anomalies.

One amusing thing about taking a data-driven approach is that we require less, and less accurate, knowledge about how stars work. Most infrared excess projects will have to deal with dust reddening, and have physically accurate models for the multi-wavelength emission from stars. We require neither; we require only that infrared excess events be around stars that are typical in the sense that there are (many) other stars in the target sample that are similar but lacking an infrared excess.

The rest of this paper is organized as follows: the data curation is described in Section 2. The method details are provided in Section 3 along with a list of subsequent cuts applied to obtain our final set of 53 candidates. Further analysis of these candidates including checking for H α emission, variability, Black Body fitting and their parameters, and rate of recovery for those, can be found in Section 4. We provide concluding remarks in Section 5. We also provide in the Appendix A a check for mid-IR deficit. The data products as well as the pipeline code and the analysis code can be found at <https://github.com/contardog/NotATechnosignatureSearch>.

2. DATA

We combine data from *Gaia* DR3 (Gaia Collaboration et al. 2016, 2023; Babusiaux et al. 2023), the Two Micron All Sky Survey (*2MASS*) (Skrutskie et al. 2006) (Skrutskie et al. 2006), the *unWISE* catalogue (Schlafly et al. 2019) and *AllWISE* catalogue (Cutri et al. 2021). We describe in this section our data curation and selection pipeline.

Using *Gaia* DR3 observations, we select stars with a *G*-band magnitude brighter than $G < 16\text{mag}$. We apply a temperature cut s.t. the effective temperature is between 4000 and 7000 K (restricting the stellar types to FGK). We impose the parallax over error to be over 10, $\text{ruwe} < 1.4$ and require that *ebpminrp_gspphot* (reddening value using BP/RP spectra) is not null. We rely on the cross-match between *Gaia* DR3 and *2MASS* (*gaiadr3.tmass_psc_xsc_best_neighbour*),

and between *Gaia* DR3 and *AllWISE* (*gaiadr3.allwise_best_neighbour*), provided by the ESA, to get the counter-part candidates in each catalogue. Using the DPAC curated catalogues available on ESA *Gaia* archive, we impose that the contamination flags (*cc_flags*) from *AllWISE* is '0000', i.e. there is no (flagged) contamination in any of the bands. We also restrict our sample to enforce that the photometric uncertainty in *2MASS* is under 0.2 for all bands, and with a *2MASS* photometric quality flag of 'AAA' (i.e. $\text{SNR} > 10$). Additional cuts to prevent potential mismatch or contamination are also applied: we enforce that the “*number of mates*” in both *2MASS* and *AllWISE* is 0 (i.e. there is no other *Gaia* sources that have this object as best neighbour as well: this should ensure (to some extent) that we do not get sources that were actually more than 1 object but unresolved in *2MASS* or *WISE*), and that the “*number of neighbours*” is equal to 1 (i.e. there is no additional source in the external catalogue that matches the *Gaia* source within position errors). Note that those cuts do not necessarily prevent potential contamination from close nearby sources if both sources were resolved in all catalogues (we suggest an additional crowding flag to address this in Section 3). Finally, we impose that the angular distance between the *Gaia* source and its best neighbours in the external catalogues is under 0.15 arcseconds. The corresponding ADQL query for this cross-match selection is provided in Figure 2. It results in a preliminary dataset of 18,751,187 stars, or roughly about 1% of *Gaia* DR3. The left panel of Figure 1 shows the distribution of this sample in the color-magnitude diagram.

We restrict this sample further by selecting stars along the main sequence, with the following colour cut:

$$0.65 < B - R < 1.5 \quad (1)$$

and a cut in the color-absolute magnitude plane:

$$3.83 \times \log(B - R) + 5.05 < M_G < 3.83 \times \log(B - R) + 5.95 \quad (2)$$

with M_G computed as

$$M_G = G + 5 + 5 \times \log_{10}\left(\frac{\varpi}{1000 \text{ mas}}\right) \quad (3)$$

where ϖ is the measured parallax.

This reduces our dataset to 5,979,478 stars. We additionally apply a dust cut, using the *dustmaps* library (Green 2018) with the SFD (Schlegel et al. 1998) dust reddening map. We discard sources with values above 1.

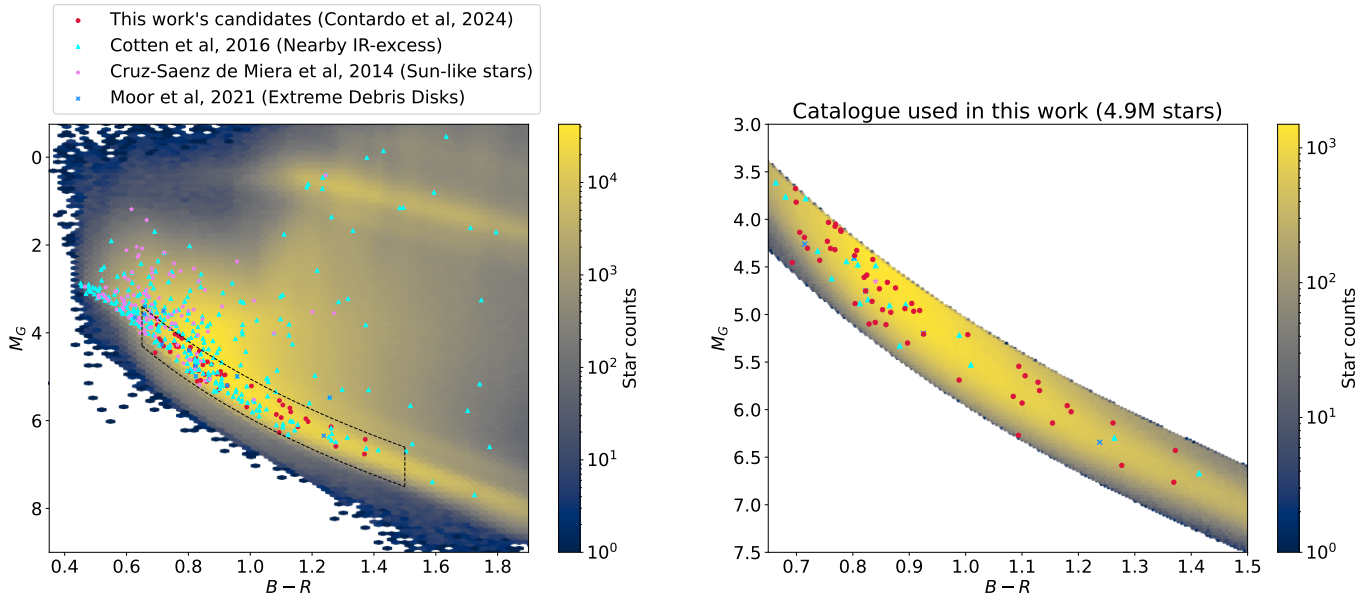


Figure 1. Left panel shows our initial sample after the SQL query (Fig 2, of 18M FGK-type stars in *Gaia* DR3 with good cross-matches in *AllWISE* and *2MASS*), in the color–absolute-magnitude space. The absolute magnitudes were computed as shown in Eq. 3, and there were no corrections made for extinction or reddening by dust here. We plot IR-excess candidates from the literature that appear in this preliminary sample: from Cotten & Song (2016) (cyan, targeting nearby stars), Cruz-Saenz de Miera et al. (2014) (pink, targeting Sun-like stars), and Moór et al. (2021) (blue, targeting Extreme Debris Disks). Our final prime set of candidates is shown in red. The dashed black box illustrates our main-sequence cut, dust cut and *unWISE* control cut as described in Section 2. Right panel shows the final sample used for our search, after our main-sequence cut, dust cut and *unWISE* control cut as described in Section 2.

We then use the cross-match service provided by the *NOIRLab*’s *Astro Data Lab* to obtain the corresponding *unWISE* values for *W1* and *W2* bands. We remove sources matched with more than one counterpart in the *unWISE* cross-match table (where the original cone-search was of 1.5 arc-seconds), and we apply a distance cut between matched sources under 0.15 arc-seconds. We control for valid values in *W1* and *W2* magnitudes and restrict our sample to stars with *unwise_flags* values of 0 for the bitmask for both *W1* and *W2* bands (i.e. sources are not deemed impacted by nearby bright sources or artefacts).

This results in a final sample of 4,898,812 million stars. The right panel of Figure 1 shows the distribution of this sample in *Gaia* color-absolute magnitude diagram.

3. METHOD

We propose to approach the problem of identifying infrared-excess stars in a data-driven fashion. Namely, our goal is to fit (or learn) a model on the data to predict the expected values for *W1* and *W2* bands, and to use the error in prediction as an indicator for anomalies, and potential infrared-excesses. Specifically, we are going to look for *confidently wrong* predictions of the model.

We use the following features as input to our model: photometric observations (magnitude) from *Gaia* DR3 and *2MASS* (*G*, *B*, *R* mean magnitudes, and *J*, *H*, *K_s*), colors computed from *Gaia* and *2MASS* (*B*–*R*, *B*–*G*, *G*–*R*, *J*–*H*, *J*–*K*, *H*–*K*, and *G*–*J*), and absolute magnitude *M_G*. We additionally use the *ruwe*, *parallax* and *ebpminrp-gspphot* features from *Gaia*.

We fit independent Random Forest (RF) regressors to predict respectively the colors *K*–*W1* and *K*–*W2*. We use the default setup from *sklearn* (Pedregosa et al. 2011a) using a mean-squared error criterion, 100 trees and no maximum depth. Comparisons with other (more flexible) models showed no improvement in prediction quality on a held-out sample, and therefore we chose this simple yet effective method.

We perform an 8-fold split, where different RFs are trained separately on each fold (12.5% of the data or about 600,000 stars). We thus get 7 “test” predictions (for which the star did not appear in the training sample) for each star in our sample, for each colour.

Using the true observed *K* magnitude, we compute the predicted *unWISE* magnitudes for a star *i* using the predicted color from the Random Forest (RF) of fold *j* as:

$$\widetilde{W}_{i,j} = -(RF_j(x_i) - K_i) \quad (4)$$

```

SELECT dr3.*, xmatch.*, allw.*, tmassmatch.*, xjoin.*, tmass.*,
dr3_all.duplicated_source
FROM gaiadr3.gaia_source_lite AS dr3
JOIN gaiadr3.gaia_source AS dr3_all USING (source_id)
JOIN gaiadr3.allwise_best_neighbour AS xmatch USING (source_id)
JOIN gaiadr1.allwise_original_valid AS allw
ON xmatch.allwise_oid = allw.allwise_oid
JOIN gaiadr3.tmass_psc_xsc_best_neighbour AS tmassmatch USING (source_id)
JOIN gaiadr3.tmass_psc_xsc_join AS xjoin USING (clean_tmass_psc_xsc_oid)
JOIN gaiadr1.tmass_original_valid AS tmass
ON xjoin.original_psc_source_id = tmass.designation
WHERE (dr3.random_index BETWEEN start_index AND end_index
AND dr3.parallax_over_error > 10.0
AND dr3.teff_gspphot BETWEEN 4000 AND 7000
AND dr3.phot_g_mean_mag < 16 AND dr3.ruwe < 1.4
AND dr3.ebpmirp_gspphot IS NOT NULL AND allw.cc_flags = '0000'
AND tmass.ks_msigcom < .2
AND tmass.h_msigcom < .2 AND tmass.j_msigcom < .2 AND tmass.ph_qual = 'AAA'
AND tmassmatch.number_of_neighbours = 1 AND xmatch.number_of_mates = 0
AND xmatch.number_of_neighbours = 1 AND tmassmatch.number_of_mates = 0
AND xmatch.angular_distance < .15 AND tmassmatch.angular_distance < .15)

```

Figure 2. Gaia ADQL query for data selection and cross-match with *AllWISE* and *2MASS* of FGK stars. This query has to be looped over ranges of *start_index* and *end_index* using *Gaia* DR3 *random_index* provided, to cover the entire *Gaia* data.

(for both $W1$ and $W2$ bands). We denote our prediction computed as the median over the folds prediction for a star i :

$$\widehat{W}_i = \text{Median}(\{\widetilde{W}_{i,j}\}_{j \in F_i}) \quad (5)$$

Where F_i denotes the folds’ indices where i is not in the training set (hence we get 7 predictions per star for each band). Using \widehat{W}_i as our predictor, we obtain a Mean Absolute Error of 0.016 for $W1$ and 0.023 for $W2$.

The left panel in Figure 3 shows our sample in the $W - \widehat{W}$ error-space. Stars with very high prediction errors can be regarded as anomalous, either in excess (negative values) or deficit (positive values), as it means that the observed magnitude significantly deviates from the model prediction. Interestingly, one can see that significant infrared *deficit* (positive values) in both bands are barely existent, as expected. We highlight as red points a set of preliminary candidates selected from a cut within that error space (dashed lines, corresponding to Equation 8 described below). We can also see in this Figure panel that there seem to be two “types” of excess candidates: one kind lying on the 1-to-1 line in terms of error in predicted magnitude, and another kind where the excess (error) is (roughly two times) stronger in $W2$, but less candidates lying in between those “groups”.

While high prediction errors indicate potential anomalies, we also want to focus our search on *highly confident* incorrect predictions. Therefore, we propose to introduce

additional criteria to flag candidates that (i) have a high prediction precision, i.e. the predictions across the folds have low variance (not dependant on the training set), (ii) are in *well predicted* regions (similar examples have a high accuracy), (iii) are in a well-populated region of the dataset (they are not outliers in the feature-space).

Precision metric—: We define the fold-MAD (Median Absolute Difference) metric for a data-point i as the median of the absolute differences between each prediction from the RFs trained on different folds, and the global prediction \widehat{W}_i :

$$\text{fold-MAD}_i = \text{Median}(\{|\widehat{W}_i - \widetilde{W}_{i,j}|\}_{j \in F_i}) \quad (6)$$

This metric can be seen as a precision metric, relying on the scatter in the predictions for the object i .

Accuracy of similar examples—: For each object in our sample, we take their K -nearest neighbours ($K = 30$) in the following feature space, in each test-fold: $H - K, G - R, J - K, G - J, B - G, M_G$, parallax, *ebpmirp* (reddening), and *ruwe*. (Those features have been identified as the “most important” features for predictions by the Random Forests). The features are rescaled in a MinMax fashion before computing the neighbours. We refer to this KNN as NN-colour. We compute the K-MAD of a star i in the test-set of fold j as the median of

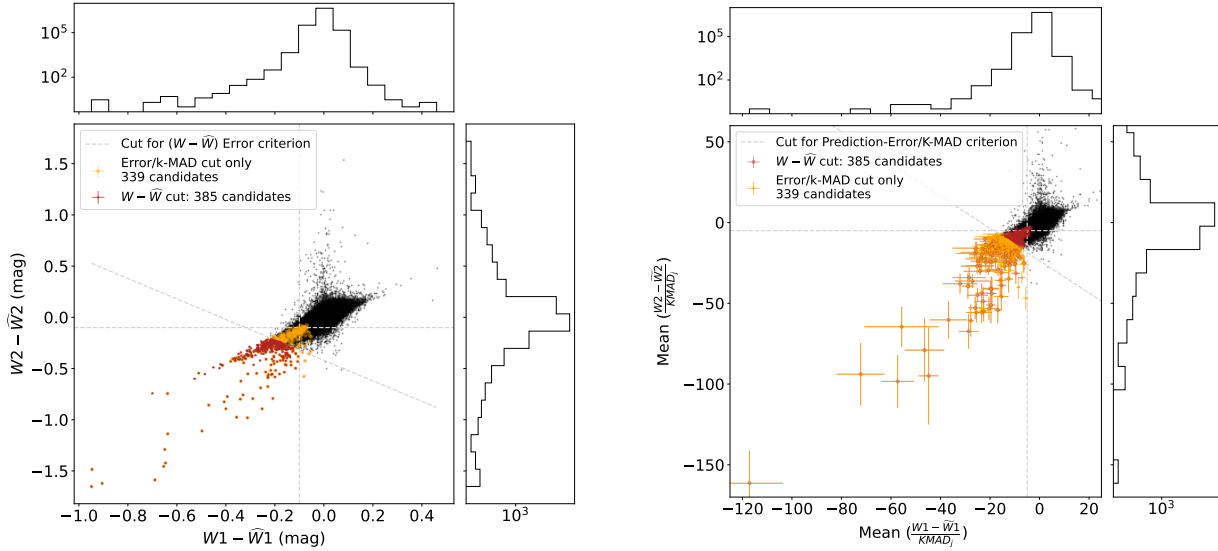


Figure 3. Left panel shows the difference between observed $W1$ (resp. $W2$ on y -axis) and the predicted $\widehat{W1}$ (resp. $\widehat{W2}$). We select stars with a high error in both bands as a preliminary sample of IR-excess candidates, depicted in red (cuts as dashed grey-lines corresponding to Eq. 8). The right panel shows the mean across 7-folds of the prediction error, divided by the Median Absolute Error of the object’s 30 nearest neighbours in the respective fold. Error bars are standard deviations across the 7-folds. We select another set of candidates in this space, depicted in orange. Red data points match the ones in the left panel, and respectively the orange points match the ones in the right panel.

the absolute differences between the true and predicted magnitudes $\widetilde{W}_{k,j}$ over the K neighbors in that test-set:

$$\text{K-MAD}_{i,j} = \text{Median}(\{|W_k - \widetilde{W}_{k,j}|\}_{k \in \text{NN-colour}(i,j)}) \quad (7)$$

Where $\text{NN}(i,j)$ denotes the K nearest neighbours indices for the object i in the test-set of fold j , and W denotes either $W1$ or $W2$ bands. In other words, this measures if similar examples to a given object are well predicted or not. We can use this to favour candidates that have high errors but a low K-MAD (i.e. candidates for which similar objects were correctly predicted), increasing our confidence in the anomalous nature of the object, or to reweight the significance of an error in prediction through the K-MAD (i.e. a small prediction error is “more significant” if the neighbours are very accurately predicted). We note however that if we had a “cluster” of, say, objects with an IR excess that were all very similar in the feature space (enough so that they’d form the majority of each others’ neighbourhood), this criterion could mechanically discard these objects. We consider however that, given the size of our sample, the feature space we look at and the rarity of the objects we are looking for, this is relatively unlikely to happen.

The right panel of Figure 3 shows the distribution of our sample in the prediction error divided by the K-MAD (computed per fold), averaged across the test-folds, for $W1$ and $W2$. We also plot the standard deviation across

the folds as error bars for a selection of infrared excess candidates (negative values) under this criterion, shown in yellow. The red candidates (high prediction errors) from the left panel of the same Figure match the red points in the right panel, and vice-versa for orange points, showcasing how some high-error sources might be significantly down-weighted by the use of the K-MAD.

Well-populated region of the feature space—: Additionally, we can compute the distance between the source and its neighbours. We can use this metric as a criterion for flagging or removing candidates that might live in a low-density region of the input feature space (hence with possibly less reliable prediction, and for which the K-MAD might not be indicative).

We propose to further investigate a set of candidate stars that are selected through a combination of the prediction error criterion (red points in Figure 3), the error over K-MAD criterion (yellow point in Figure 3, down-weighting the points that are in a region of the feature-space that is badly predicted, favouring high-accuracy regions), and the fold-MAD, to ensure our candidates have small prediction uncertainties (low scatter). More specifically, we select the stars with an error in each band under the 0.008-th percentile value (dashed light-grey diagonal line in the left panel of Figure 3), and with both errors under -0.1 mag:

$$\begin{aligned}
(W1_i - \widehat{W1}_i) + (W2_i - \widehat{W2}_i) &< -0.42 \\
(W1_i - \widehat{W1}_i) &< -0.1 \\
(W2_i - \widehat{W2}_i) &< -0.1
\end{aligned} \tag{8}$$

For the error over k-MAD cut, we similarly select stars with a sum of the mean of error over k-MAD under the 0.007-th percentile value, and with both means of error over K-MAD under -5 :

$$\begin{aligned}
\frac{1}{7} \sum_{j \in F_i} \frac{(W1_i - \widetilde{W1}_{i,j})}{\text{K-MAD1}_{i,j}} + \frac{1}{7} \sum_{j \in F_i} \frac{(W2_i - \widetilde{W2}_{i,j})}{\text{K-MAD2}_{i,j}} &< -23.59 \\
\frac{1}{7} \sum_{j \in F_i} \frac{(W1_i - \widetilde{W1}_{i,j})}{\text{K-MAD1}_{i,j}} &< -5 \\
\frac{1}{7} \sum_{j \in F_i} \frac{(W2_i - \widetilde{W2}_{i,j})}{\text{K-MAD2}_{i,j}} &< -5
\end{aligned} \tag{9}$$

We additionally select candidates that have a fold-MAD under 0.01 mag:

$$\begin{aligned}
\text{Median}(\{|\widehat{W1}_i - \widetilde{W1}_{i,j}|\}_{j \in F_i}) &< 0.01 \\
\text{Median}(\{|\widehat{W2}_i - \widetilde{W2}_{i,j}|\}_{j \in F_i}) &< 0.01
\end{aligned} \tag{10}$$

This results in a preliminary set of excess candidates of 127 stars.

3.1. Additional cuts to reduce false-detection by contamination and other artefacts

On those objects, we evaluate the following additional features that could lead to false anomalies:

- **Crowding:** For each object, we perform a cone-search in *Gaia*, *2MASS*, and *unWISE* catalogues of 5 arcseconds. If another object is found within that cone for any of the catalogues, we flag it as potentially being contaminated, or in a crowded area.
- **Figure of Merit (FoM) from *Gaia*:** Following the recommendations in Dennihy et al. (2020) to alleviate source confusion when looking for IR-excess in *WISE*, we check the figure of merit (*score*) provided by ESA *Gaia* cross-match with *AllWISE*. This score assesses the quality or ‘like-likeness’ of the match (the higher the better), however, it is not normalized. Dennihy et al. (2020)

suggest as a rule of thumb to discard sources with a high SNR but a low FoM (they suggest that excesses with $\text{SNR} > 10$ but $\text{FoM} < 4$ are likely the result of source confusion). We do not have objects with a FoM under 4 in our preliminary set of candidates.

- **Proper-Motions Comparison:** Dennihy et al. (2020) also suggest to check proper motions agreements between catalogues to remove potential source confusion. They indicate that the proper motion accuracy in *CatWise* depends on the magnitude of the source (10 mas yr⁻¹ for bright sources, 30 mas yr⁻¹ for $W1 \approx 15.5$ mag). We therefore compare the proper motions from *Gaia* and from *CatWise*, and apply a cut when the proper motions in either *RA* or *DEC* disagree more than the approximated accuracy for the source brightness.
- **Disagreement between *unWISE* and *AllWISE*:** To ensure confidence in the observed magnitude of our targets, we add a flag checking for agreement between *unWISE* and *AllWISE*. *unWISE* documentation recommends subtracting 4 mmag from *unWISE* W1 and 32 mmag from *unWISE* W2 to improve agreement between both catalogues. After doing so, we add an ‘agreement-flag’ such that $|W^{AllWISE} - W^{unWISE}| < 0.15$ for both bands.
- **Distance to galactic plane:** We remove candidates that are close to the galactic plane s.t. $abs(b) > 10$.
- **Binary and duplicated sources:** Candidates that are indicated as ‘non single stars’ by *Gaia* DR3 are flagged. We also check each candidate with Simbad, and flag each star that is indicated to be eclipsing binaries or eclipsing binaries candidates. *Gaia* DR3 also provide a *duplicated source* flag (which may indicate observational, cross-matching or processing problems, stellar multiplicity, and possible unreliable astrometry or photometry). We therefore discard candidates with this flag.

We combine these different flags to obtain a curated final set of 53 MIR-excess candidates. We provide in Table 1 the number of candidates remaining after applying each cut. The *Gaia* DR3 and *2MASS* ID of those 53 candidates are available as a csv file at <https://github.com/contardog/NotATechnosignatureSearch> along with the code for this pipeline and the following analysis.

Table 1. Table of criterion for our candidates selection, and the number of candidates remaining after each cut.

| Criterion cut | Number of remaining candidates |
|---|--------------------------------|
| Prediction Error cut (Eq. 8) | 385 |
| Mean (Prediction Error / k-MAD) cut (Eq. 9) | 339 |
| Error cut AND error/k-MAD cut | 170 |
| fold-MAD cut (Eq. 10) | 127 |
| Crowding cut at 5 arcsecond | 87 |
| FoM > 4 cut | 87 |
| Proper-Motion disagreement cut | 78 |
| Disagreement <i>AllWISE/unWISE</i> cut | 76 |
| Mean Distance k-NN < .1 | 66 |
| $abs(b) > 10$ | 59 |
| Removing binaries and binaries candidates (<i>Gaia</i> , Simbad) | 55 |
| Removing duplicated sources (<i>Gaia</i> DR3 flag) | 53 |

4. ANALYSIS OF EXCESS CANDIDATES

4.1. *Overlap with previously detected IR-excess*

We check our pipeline selection and list of candidates against existing IR-excess candidates from the literature. We summarize this search in Table 2. For each reference investigated, we retrieve catalogues from either SIMBAD or Vizier, retrieve the *Gaia* DR3 match from SIMBAD if there is one (second column), and check if those objects are in our full 4.9M sample (third column). We indicate which of those objects make it through our preliminary cut (combining Equations 8,9 and 10) (fourth column) and through the complete pipeline (fifth column). Note that some objects in those catalogues might not be matched yet with a DR3 identifier and could thus actually appear in our sample.

The excesses most similar to our candidates are likely to be Extreme Debris Disks candidates, and we indeed find that these objects are the ones that most often make it through our preliminary cut. Out of 23 objects matched from the catalogue available on SIMBAD², 5 appear in our full sample, and they all make it through our preliminary cut, confirming the ability of our pipeline to detect such IR-excesses. Two of those are then discarded by the crowding cut, one is discarded by the proper-motion disagreement cut, and one by the k-NN “density” cut.

² We note that the original paper however mentions 17 candidates.

One remains in our final set of candidates, *Gaia* DR3 2942418533272205312 (bottom left plot in Figure 16).

Out of the few other IR-excess candidates appearing in our 4.9M sample (42 in total), only one passes through the preliminary cut (from the Reserved catalogue by Cotten & Song (2016)), but is discarded by the crowding criterion.

This encourages us to believe that we explored a large sample of stars relatively disjointed from previous searches, both in the population sample analyzed (little overlap in the main catalogue) and in the type of excess detected. It is relevant to note that the IR-excesses in the literature were detected in *W3* and *W4* bands, and hence might not produce an excess in the MIR detectable by our pipeline. It also requires stringent cuts on the quality and SNR of *W4*, which eliminates a large number of objects. Our detection pipeline allows for the discovery of extreme outliers (similar to potential EDDs) by relying on *W1* and *W2* bands only, while being rather conservative in further removing potential false detection.

4.2. *Characterization of the hosts*

We provide in Figure 4 histograms of our candidates’ sample and of our complete sample in $B - R$, $[M/H]$, Teff, and M_G . We observe a gap in our candidates’ distribution around 1 in $B - R$, 5.5 in M_G and 5400K in Teff. There also seems to be an over-density in our candidates’ distribution compared to the full sample of

Table 2. Table of overlap between existing IR-excess catalogues and our sample and set of candidates. We retrieve the DR3 identifiers counterparts of the candidates using SIMBAD and indicates the number of objects in our full sample and the number of objects passing the preliminary cut and the full pipeline selection.

| Reference | Objects with DR3 match | Objects in our 4.9M catalog | Preliminary Cut | Full Cut |
|--|---------------------------|--------------------------------|-----------------|----------|
| Extreme Debris Disk (Moór et al. 2021) | 23 | 5 | 5 | 1 |
| Cotten & Song (2016), Prime | 491 | 0 | 0 | 0 |
| Cotten & Song (2016), Reserved | 1218 | 18 | 1 | 0 |
| Sun-Like stars (Cruz-Saenz de Miera et al. 2014) | 199 | 1 | 0 | 0 |
| Main-Sequence (Da Costa et al. 2017) | 210 | 6 | 0 | 0 |
| Tycho-Gaia DR1 McDonald et al. (2017) | 3836 | 16 | 0 | 0 |
| Cold Debris Disk Spitzer (Ballering et al. 2013) | 225 | 0 | 0 | 0 |
| T-tauri (Manzo-Martínez et al. 2020) | 784 | 1 | 0 | 0 |
| Herbig Ae/Be (Arun et al. 2019) | 121 | 0 | 0 | 0 |
| Cepheids (Schmidt 2015) | 27 | 0 | 0 | 0 |

stars with colour $B - R < 0.9$. Because of the data-driven nature of our approach, the subsequent cuts used to create our candidates’ sample, and the small size of our final sample, it is hard to give clear interpretations and conclusions about these trends. We note however that the dip observed here at $B - R \sim 1$ is not strongly visible when looking at the distribution of the candidates selected using the Prediction Error only (Eq. 8) or the k -MAD cut only (Eq. 9), and only start appearing when combining Eqs 8, 9 and 10 altogether, and is further depleted by subsequent cuts (at a somewhat similar rate than other color-bins), but those are small numbers statistics. We also observe an off-set trend in M/H towards lower values than the full sample, with a few outliers standing out.

4.3. H -alpha emission

Our sample focuses on the main sequence, but stars might have only recently joined and could be in a “transitional” phase between protoplanetary disks and debris disks (Wyatt et al. 2015). To properly understand the nature(s) of the excesses observed in our candidates, and to identify the most interesting candidates for follow-up observations (e.g. confidently old stars with an unusually high IR excess), it is crucial to constrain the hosts’ ages. We investigate different markers that could indicate that the host is young or recently joined the main sequence. However, the analysis presented below is only a first step and we defer thorough age-estimations of the candidates to future work.

To investigate the potential “youngness” of our candidates, we start by evaluating the $H\alpha$ emission. We first

use the measurement of the pseudo-equivalent width of the $H\alpha$ line provided by *Gaia* DR3 from the RP spectra, *ew_espels_halfalpha*. The value is expected to be negative when emission is present. The left panel of Figure 5 shows the distribution of this measurement for our candidates’ sample (dark red line), as well as a randomly selected control sample of 1,600 stars from our 4.9M sample (blue) and a set of stars similar to our candidates called “Neighbors” (dashed black line). This set of neighbours is computed in a different features-space than previously. We use the following features to favour stars of similar magnitude and spectral shape (while our previous KNN relied on colour): M_G , *ebpminrp_gspphot*, *parallax*, *ruwe*, G , J , H , Ks , B , and R . We refer to this KNN as NN-mag.

We can see two clear outliers in our set of candidates with high $H\alpha$ emission, indicating young stellar objects. The rest of our candidates seem to follow the control distribution, perhaps with a slight over-density on the absorption side.

As a sanity check, we perform a different measurement of potential emissions or absorptions of $H\alpha$ as follow: using the XP spectra and *GaiaXP* library, we measure the flux value of the spectra at the $H\alpha$ wavelength (656.46nm). For an object i , we obtain the flux values of its 30 nearest neighbours (using NN-mag), and compute the difference between the object’s flux and the median flux of its neighbours, divided by the median flux:

$$E_{H\alpha,i} = \frac{F_{H\alpha,i} - \text{Median}_{k \in \text{NN-mag}(i)}(F_{H\alpha,j})}{\text{Median}_{k \in \text{NN-mag}(i)}(F_{H\alpha,j})} \quad (11)$$

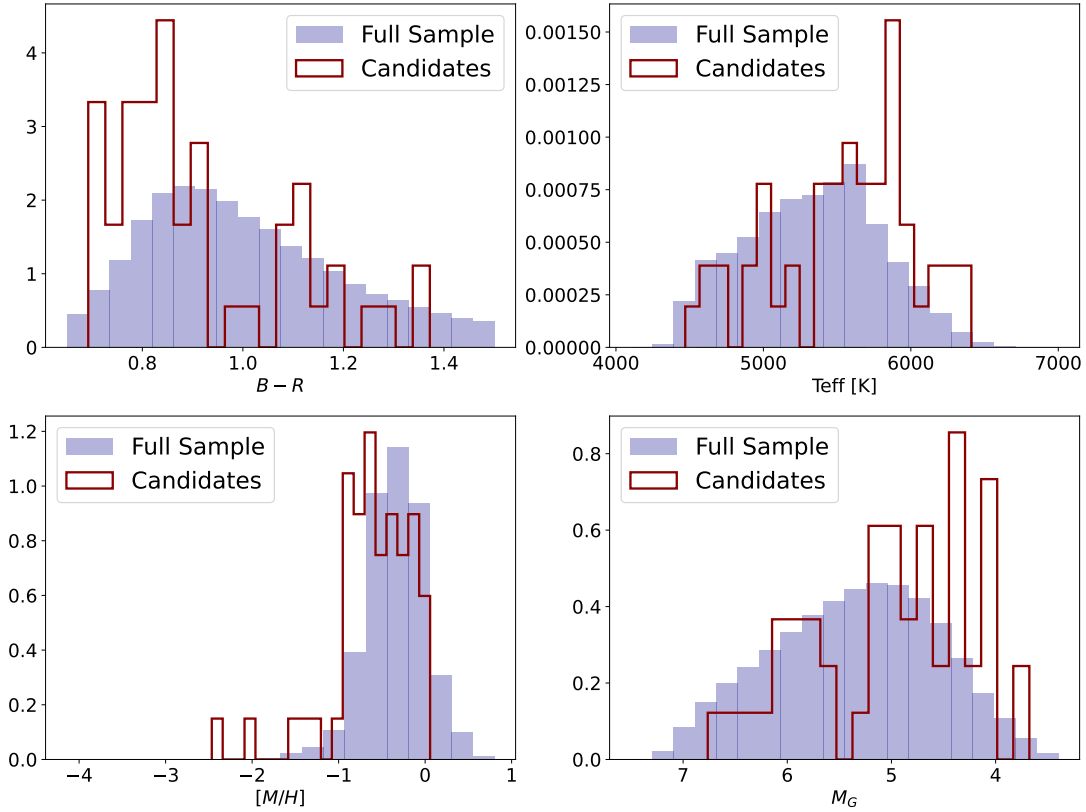


Figure 4. Histograms of distribution of our candidates’ sample (dark red outline) and our full 4.9M stars sample (blue) in $B - R$, effective temperature, $[M/H]$, and M_G .

This metric provides an indicator of how much the object flux diverges at the $H\alpha$ line from similar objects, where a positive value would indicate emission (respectively absorption for negative values). The middle panel of Figure 5 shows the distribution of $E_{H\alpha}$ for our set of candidates, the control sample and the neighbours sample, and the right panel shows $E_{H\alpha}$ against the pseudo-width provided by *Gaia* data product. We see agreement especially in the detection of the two high emissions objects, *Gaia* DR3 5260430146906778624 (top right panel in Figure 14) and *Gaia* DR3 3004530769758177280 (third row, left panel of Figure 15). Note that the second object corresponds to our candidate with the highest fractional luminosity (~ 0.1).

Visualizing the XP spectra also highlights some odd objects, see for instance the top middle candidate in Figure 13 (*Gaia* DR3 6705842630930258816).

For the sake of completeness and using the data product available with the catalogues we used, we also provide in Figure 6 a visualization of the age estimates provided by the Final Luminosity Age Mass Estimator (FLAME) within *Gaia* (Creevey et al. 2023) for our candidates and control samples. The “error bars” correspond to the lower and upper confidence levels of the

FLAME’s age estimates (i.e. the 16th and 84th percentile value of the 1D projected distribution from sampling in mass and age). The x -axis is the “evolution stage” from FLAME, where 100 corresponds to Zero Age Main Sequence (ZAMS), 360 to the main sequence turn-off, and 490 would be the base of the Red Giant Branch (Hidalgo et al. 2018). However, Creevey et al. (2023) highlights that those age estimates assume some prior on the metallicity, and the authors advise caution in using those ages for stars outside of the $-0.5 < [M/H] < +0.5$ regime. Therefore, we only plot in Figure 6 the stars in their respective sample that have a metallicity estimate (provided by *Gaia*) in this range. This selection removes all the candidates with an estimated age under 2 Gyr. However, one of the candidates with a high $H\alpha$ emission has an age estimate of 5.79 Gyrs (the other candidate does not have an estimate). We therefore recommend cautiousness in making any conclusion from those estimates.

4.4. Variability of hosts

Another potential indicator of youthness, and a matter of interest for potential sources of IR-excess, is the variability of the object. Following Moór et al. (2021),

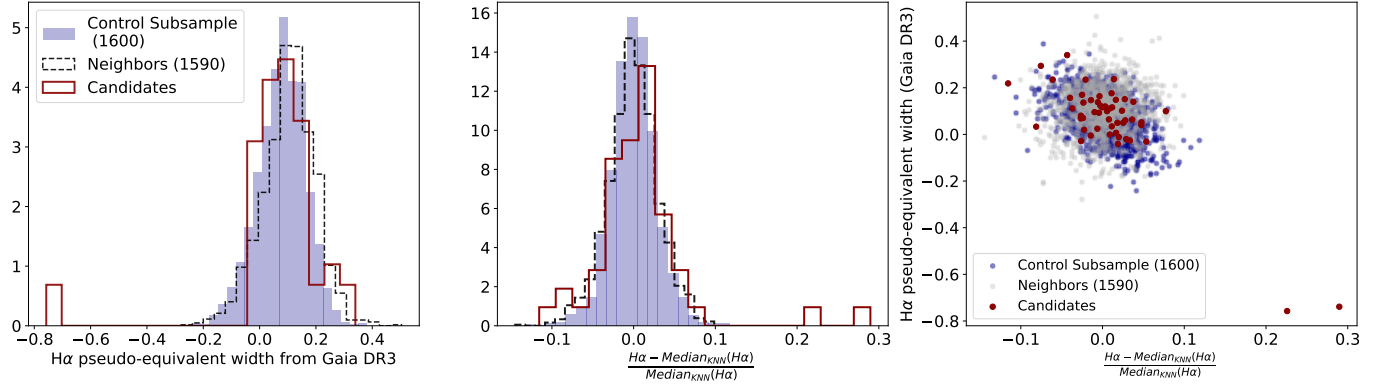


Figure 5. Distribution of measurements for H α emission for a random control subsample (blue), a set of stars similar to our candidates (black dashed line) and our candidates set (dark red line). Left panel shows the distribution of the pseudo-equivalent width of the H α line provided by *Gaia* DR3 (negative values indicate emission). Middle panel shows our measurement using Equation 11 (positive values indicate emission). Right panel shows those measurements against each other.

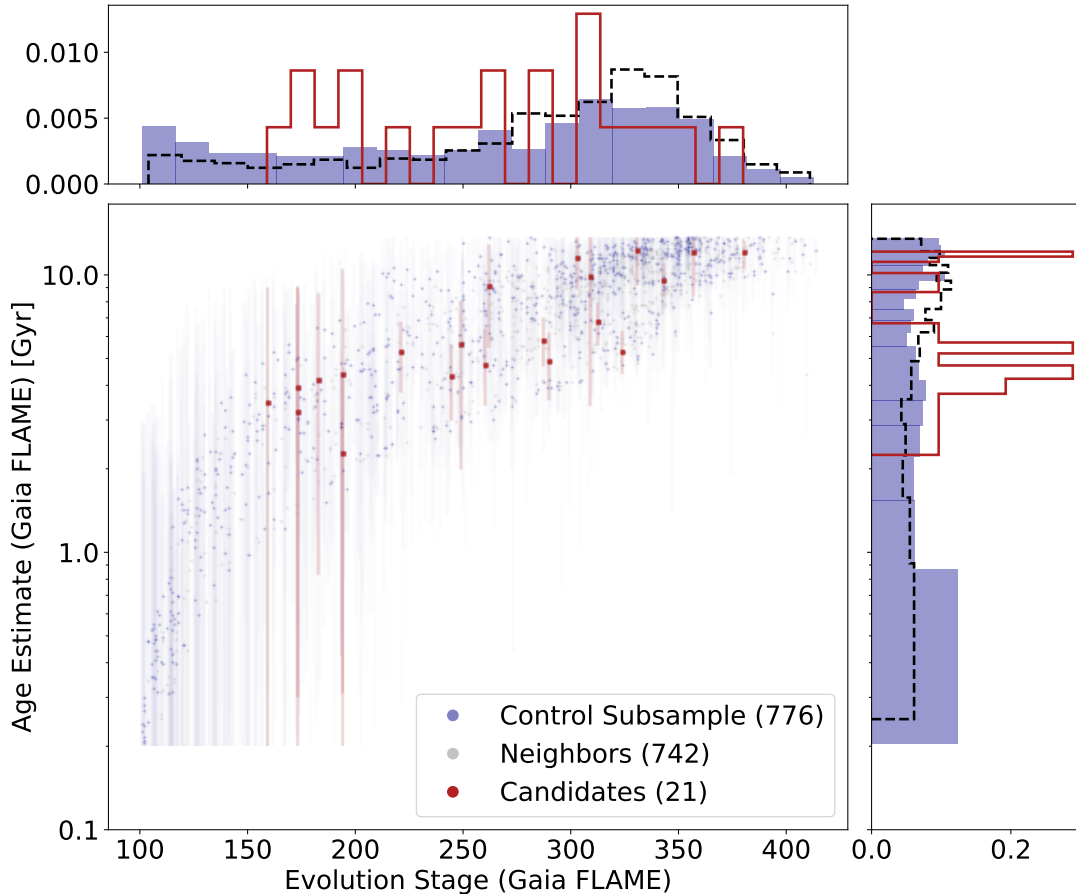


Figure 6. Age estimates and evolution stage provided by the Final Luminosity Age Mass Estimator (FLAME) in *Gaia* DR3, for our candidates (dark red), a set of similar stars (grey) and a control sample (blue), restricted to the stars that have $-0.5 < [M/H] < +0.5$. The error-bars depict the lower (16th percentile) and upper (84th percentile) ages to cover the 68% confidence interval. The x -axis Evolution Stage goes from 100 (Zero Age Main Sequence) to 490 (Red Giant Branch). 360 would be the main sequence turn-off.

we use the *NeoWISE* time series to investigate first the variability of our candidates in the mid infrared. We use the correlation-based Stetson index (Stetson 1996) S_J , which measures the correlation of the variability in two (or more) bands and can be computed for a given object as follows:

$$S_J = \frac{\sum_{j=1}^n w_k \text{sgn}(P_k) \sqrt{|P_k|}}{\sum_{j=1}^n w_k} \quad (12)$$

Where n is the number of paired observations across the different bands, w_k is a weight per epoch (uniform in our case) and :

$$P_k = \left(\sqrt{\frac{n}{n-1}} \frac{W_{1,k} - \bar{W}_1}{\sigma_{W_{1,k}}} \right) \left(\sqrt{\frac{n}{n-1}} \frac{W_{2,k} - \bar{W}_2}{\sigma_{W_{2,k}}} \right)$$

Where $\sigma_{W_{i,k}}$ is the uncertainty for the k -th observation in the i -th band, and \bar{W}_i is the mean of the observed points in band i .

We compare the Stetson index obtained by our candidates against a random control sample and a set of neighbours (computed with NN-colour), shown on the left panel of Figure 7. We observe a small overdensity for higher Stetson index in our candidates' set, highlighting these candidates as potentially (more) variable objects. The object with the highest Stetson index also corresponds to an object flagged as variable from *AllWISE*'s data *var_flag*. However, the rest of our candidates have low variability scores according to this flag (in the IR). To further get a sense of the variability of our candidates, we also measure their Stetson index percentile score (right panel Figure 7) with respect to the Stetson indexes of the control sample (in blue), and with respect to their 30 neighbours (dashed black line).

In addition, we check the photometric variable flag provided by *Gaia* (computed in the G band). 10 out of our 53 candidates are flagged as variable, the remaining have not been processed (flag not available, hence they can not be considered not-variable either). This is a significantly larger occurrence of variable objects ($\sim 19\%$) compared to the occurrence rate in our control sample ($\sim 7\%$), the ‘‘neighbours’’ sample ($\sim 2.5\%$), and our entire sample ($\sim 5.3\%$). According to the variable classification pipeline (Rimoldini et al. 2023) provided by *Gaia*, one of our candidates is an eclipsing binary (*Gaia* DR3 6705842630930258816). Two objects are (tentatively) classified as RS Canum Venaticorum variable (*Gaia* DR3 3183786280737192704 and 2256421065353454464), one as a δ Scuti or γ Doradus or SX Phoenicis star. Four remaining are flagged as ‘‘solar like’’.

Using the cross-match of *Gaia* DR3 with known variable sources in the literature, provided by Gavras et al.

(2023), we identify two candidates classified as Eclipsing, one that was previously identified as such above by the *Gaia* variable flag and *Gaia* DR3 5260430146906778624.

Longer light curves in the optical can be obtained for some of these objects from *TESS* mission. However, a deeper analysis of e.g. periodicity and conducting gyrochronology, will require a careful pre-processing and detrending of those data, which we defer to future work. Observations from the Zwicky Transient Facility (ZTF) could also be leveraged: using the SNAD viewer (Malanchev et al. 2023), which also provides cross-matches across multiple catalogues and additional variability detection from various pipelines, we retrieve a larger fraction of our candidates compared to *TESS*.

4.5. Characterization of the Excesses through SED-fitting

We now further investigate our curated set of 53 candidates to derive properties of the possible source of excess.

First, we use *Ariadne* package (Vines & Jenkins 2022) to perform Spectral Energy Distribution (SED)-fitting on each of our candidates. Given RA,DEC positions and optionally a *Gaia* DR3 identifier, *Ariadne* automatically retrieves the object’s photometric observations from *Gaia* DR2, *AllWISE*, *APASS*, *Pan-STARRS1*, *SDSS*, *2MASS*, *ASCC*, *IRAC/GLIMPSE*, *TESS*, *SKYMAPPER*, *GALEX*, and *Tycho-2*. *Ariadne* also incorporates priors for interstellar extinction parameter through dust maps. We use the default setup relying on SFD dustmaps (Schlegel et al. 1998). The goal of *Ariadne* library is originally to improve SED-fitting through bayesian model averaging of different models. However, in the following of our analysis, we will use a single SED-model, the Castelli-Kurucz (Castelli & Kurucz 2003). We also use the ‘fitzpatrick’ extinction-law in *Ariadne* setup. *Ariadne* then returns the best-fitted SED as well as estimated stellar parameters (T_{eff} , $\log g$, distance, A_V , metallicity and radius). *Ariadne* uses by default all observed photometry up to $W2$ for the fit, but not $W3$ and $W4$.

We follow this pipeline, using *Gaia* DR3 values as priors for T_{eff} and $\log g$. However, we force the removal of the *WISE* values. The motivation is two-fold: (i) we put the SED-modeling in a similar context as our model, (ii) since we will use the fitted SED to compute properties of the potential source of the excess, we do not want to bias the predicted values in the *WISE* bands.

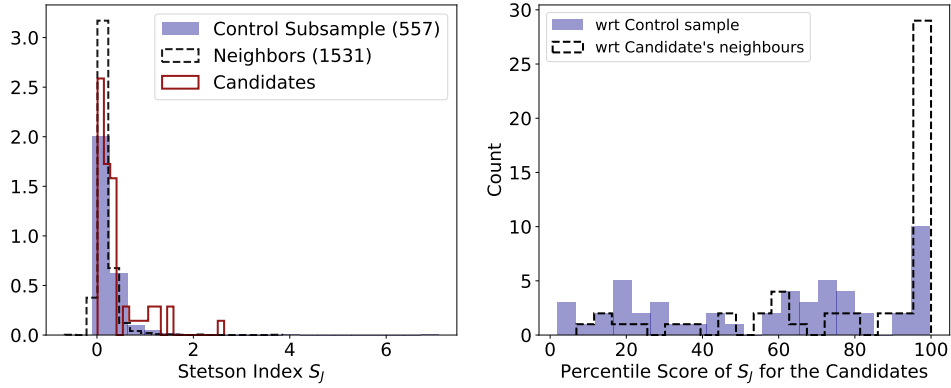


Figure 7. Left panel shows the distribution of the Stetson index (Equation 12) of our control sample (blue), of a set of stars similar to our candidates (black dashed line) and of our candidates (dark red line). Right panel shows the distribution of the percentile score of our candidates’ Stetson index with respect to the control sample (blue) and with respect to their set of similar stars (black dashed line).

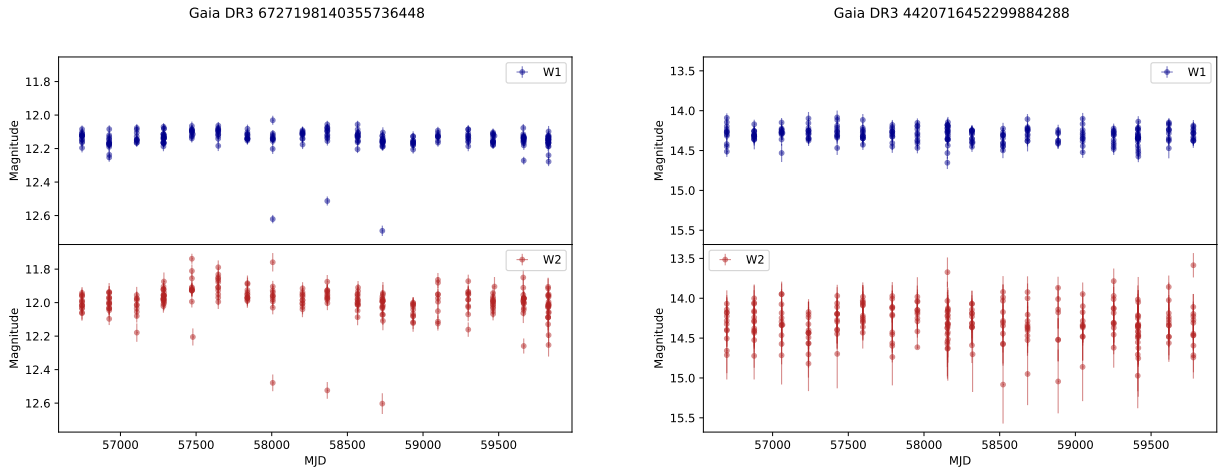


Figure 8. *NeoWISE* time-series for two of our candidates, in *W1* (blue) and *W2* (red) bands. Left panel shows a candidate with a high percentile score with respect to the control sample. Right panel shows a candidate with a low percentile score.

We obtain, for each of our candidates, SED-predicted values for all the *WISE* bands. Note that these values use potentially more observations at different wavelengths than our model, and rely on stellar model, extinction and other priors (contrary to our entirely data-driven predictions). We show in Figure 9 the flux value observed in *W2* band versus the flux predicted by the SED-fit as red points, confirming excess for all of our candidates (lying under the 1-to-1 dashed line).

Using the SED-predicted fluxes and the observed ones, we can estimate the properties of a blackbody fitted on the residuals. To do so, we build a grid of blackbody spectra with a range of temperatures from 100K to 1500K with a step of 5K, and a range of angular sizes from 10^{-23} to 10^{-16} with 200 bins spaced evenly on log-scale. For each candidate, we select the blackbody that minimizes the sum of the squared errors

as: $\text{argmin}_{BB} \sum_j (F_{BB}(\lambda_j) - (F_{obs}(\lambda_j) - F_{SED}(\lambda_j)))^2$ where j denotes an index on wavelengths. We fit the blackbody using four wavelengths corresponding to *Ks*, *W1*, *W2*, and *W3* bands. Figure 9 shows as blue dots the flux in *W2* of the SED with the additional blackbody, against the observed flux. Our fitting procedure tends to over-correct in the *W2* band, but not in *W1* and *W3*. Figure 10 shows the SED from *Ariadne* (dashed red line) and the black body fitted (dashed light grey line) for one of our candidates.

Figure 11 show the different black bodies (BB) properties we obtain (bearing in mind that those are approximate fit) with our candidates’ sample. The fractional luminosities $f_{BB} = \frac{L_{BB}}{L_*}$ (computed as the ratio of the integrated flux of the sole black body and the integrated flux of the predicted SED) range between 0.005 and 0.1, with an average of 0.02. These fractional luminosities

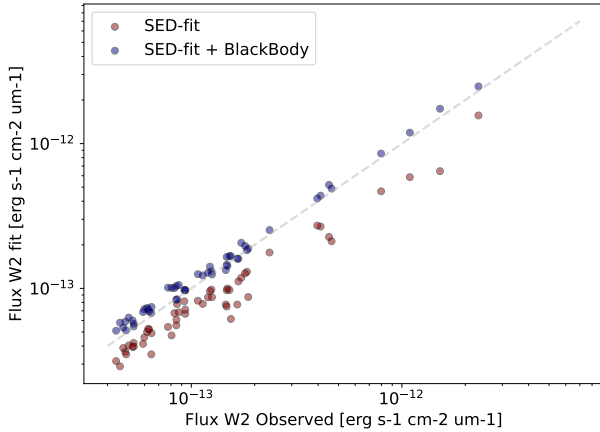


Figure 9. Observed flux (in $W2$ band) vs predicted flux from *Ariadne*-SED only (red points) and *Ariadne*-SED + a BlackBody (blue points), fitted on the flux residuals in bands Ks , $W1$, $W2$ and $W3$. The 1-to-1 line is depicted as a dashed grey line.

align with what has been observed and expected for Extreme Debris Disks candidates.

The SED and black-body fits for all of our candidates are shown in Figures 13-16, along with their XP spectra ($H\alpha$ line indicated in blue) and imaging visualization of the objects in $W1$ and $W2$ bands using *AllWISE*, and in the optical using the Digitized Sky Survey (DSS), on $3'$ square. We observe in these Figures a diversity of “excess shape” and strength: we see candidates with some extreme “bumps” in $W3$ – which are often not well fitted by our black body estimates –, similar to EDDs candidates. However, as we also display the photometric quality flag of $W3$ and $W4$ from *AllWISE*³, we can see that for some of those objects, the $W3$ band might not be reliable. This might also impact the relevance of our BB parameters fit. We also note that while these candidates might not all be EDDs, they might interestingly fall in a region of debris disks evolution and parameter space that was scarcely populated previously and provide an interesting continuum of disks’ evolution: Wyatt et al. (2015) proposed a five steps classification in the evolution of disks (from protoplanetary to debris), based on a number of a factor including flux ratio at different wavelengths (see Fig. 1 in Wyatt et al. (2015)). Our candidates would fall around HD 141569 for the flux ratio at $12\mu m$. However, the lack of reliable observa-

³ The quality flag is *A* if a source is detected with a flux SNR > 10 , *B* if $3 < \text{SNR} < 10$, *C* if $2 < \text{SNR} < 3$, and *U* if $\text{SNR} < 2$, indicating upper limit on magnitude: the magnitude of the given band is a 95% confidence upper limit. All our excess candidates have an *A* quality flag for $W1$ and $W2$.

tions at higher wavelengths, dust mass estimates, and, as mentioned previously, reliable age estimates, prevent us from placing our candidates in this classification scheme accurately. Additionally, the work conducted in Wyatt et al. (2015) focused on A stars, while our candidates are FGK stars, which might make direct comparison difficult. This motivates nonetheless further observations on this sample to better connect and understand those potential transitional objects.

4.6. Recovery Rate of Injections

As a sanity check, we perform a set of injections to evaluate the recovery rate of our pipeline depending on BB’s parameters. We select as a sample of stars the set of neighbours (in colour space using NN-colour) of our candidate, ~ 1500 objects. We create a grid of BB parameters, where the temperature ranges from 200 to 1575K by step of 25K, and the angular size ranges from 10^{-23} to 10^{-16} with 50 bins in log-scale. Each star in the sample is injected with all BBs, creating an artificially injected dataset of 4.3M objects. We only consider here the recovery as passing the cut of the first three masks used in this paper relying on prediction error (Eq 8), the confidence of error compared to similar objects (Eq 9) and the precision criterion (Eq 10). Figure 12 shows the resulting recovery rate for each temperature-angular size bin, and our candidates as the cyan points. Some of our candidates’ estimated BB parameters lie in a low or no-recovery region: this is very likely explained by the fact that our BB’s parameters estimation is done with four observations, and often a rather approximated fit (as can be seen in Figures 13-16).

It is also important to note that our selection pipeline relies in the first cut on rather arbitrarily chosen thresholds (Equations 8-10): relaxing these choices and threshold might lead to more detections and higher recovery rates of fainter MIR-excess, but also potentially to an increase in the false detection rate.

5. DISCUSSION

We proposed and executed a data-driven approach for the discovery of infrared (IR) excesses around stellar objects, more specifically among main-sequence FGK stars. We used robust machine learning methods to bypass stellar modelling to estimate the “expected” mid-IR (MIR) magnitudes, and we designed a set of curated statistics derived from the predictions and the predictions’ quality to define a set of criterion cuts. We combined those with additional cuts to prevent as much as possible false detection and artificial excess due, e.g., to

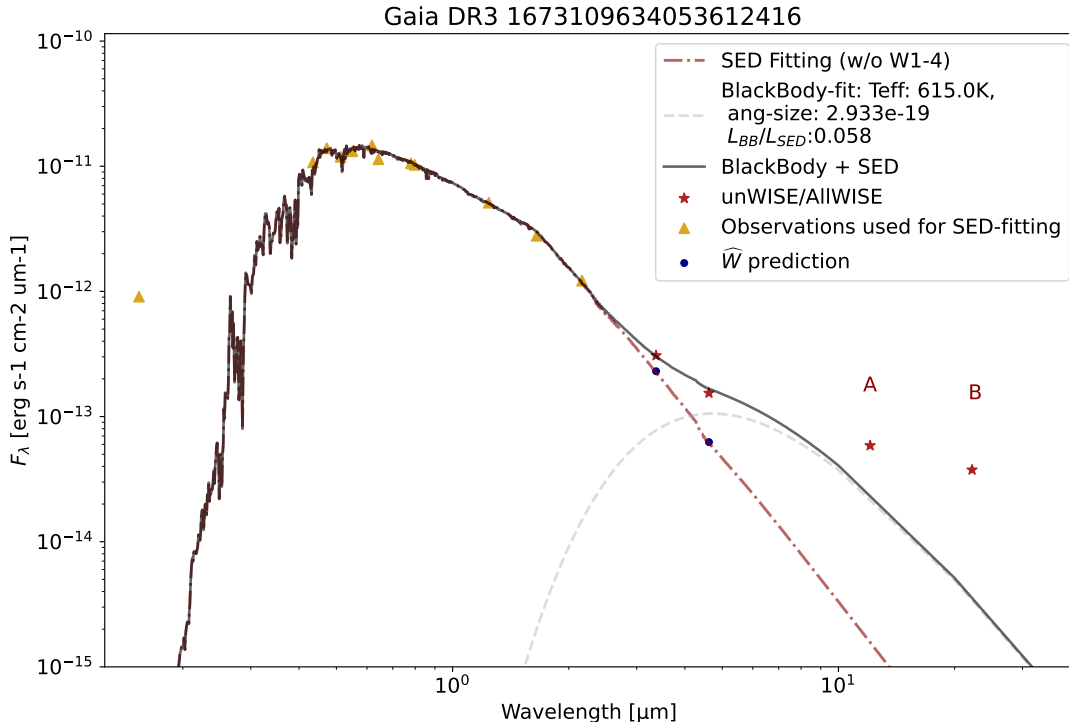


Figure 10. SED and BlackBody fitting for our excess candidates. Yellow triangles are the observations gathered and used by *Ariadne* to compute the SED (dashed dark red line). Red points are the *unWISE* (for *W1* and *W2*) and *AllWISE* (for *W3* and *W4*) values. Blue points are the prediction of our model (averaged over the 7-folds). The best-fit blackbody is depicted as grey dashed line. The final SED computed as *Ariadne* SED + BlackBody is depicted as solid black line. The letters above *W3* and *W4* are *AllWISE* photometric quality flag.

contamination. We obtained a set of 53 candidates that display interesting (M)IR excess. A few of those objects appear to be young stars (showing high $H\alpha$ emission). A significant fraction of our candidates seem to have variability in the optical, and some in the mid-infrared. This can also indicate youth, but a proper age estimation using gyrochronology and a variability analysis is required. Using SED-fitting and fitting black bodies on the flux residuals in 4 bands (*K*, *W1*, *W2*, *W3*), we compute black body properties and obtain estimated fractional luminosities coherent with the ones associated with Extreme Debris Disks (EDDs). While they might not all be EDDs, these objects form an interesting pool of potential transitional disk candidates to investigate further.

It’s natural to follow this work by gathering follow-up observations of the candidates, to confirm their nature (or discard potential confounding factors), to obtain better estimates of the properties of those disks, their compositions and their underlying processes. For example, Moór et al. (2024) recently investigated the presence of solid-state features around $10 \mu m$ in eight EDDs, and divided them into silica or silicate-dominated groups. Another key aspect will be to perform a deeper analysis to obtain reliable age estimates: the most interesting ob-

jects (as in: the ones that would challenge current models the most or would be the least expected) would be non-young. Additionally, identifying potential trends (if any) between those excesses and stellar ages might help better understand and constrain the underlying physical processes leading to such excesses.

However, we want to emphasise that while such a pipeline is relevant to identify a set of outliers candidates, it can only find (contextual) outliers according to *the data*. Making population statements (e.g. “true” occurrence rate of EDDs) is not trivially doable with this approach, as it relies heavily on a series of (sometimes arbitrarily chosen) threshold cuts to build the candidate sample. Additionally, since our model computing the “expected (M)IR magnitude” is data-driven, we cannot directly use the error in prediction as the true IR excess (or deficit) for the full sample to investigate for instance the fraction of different levels of IR excess. We also note that, in principle, the prediction errors can be due mainly to variance in the data (and hence the model not being perfectly accurate) and might not necessarily indicate “interesting anomalousness”. Here we can benefit from the fact that we are looking for the largest deviations, we expect (and have) a small sample

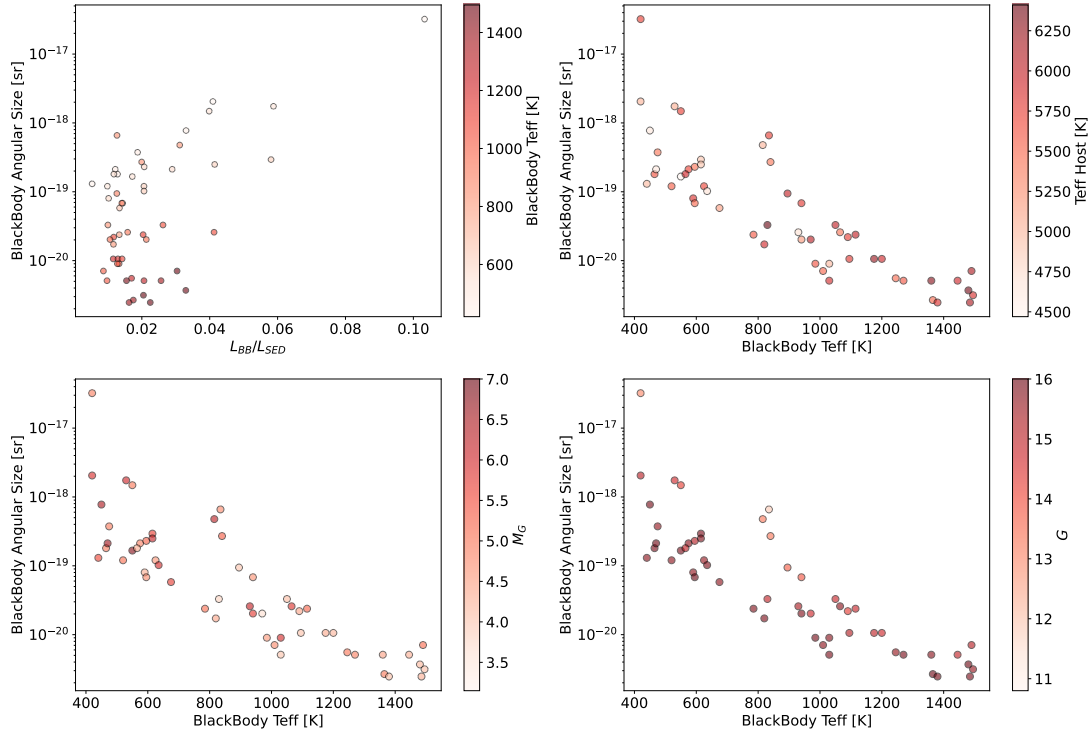


Figure 11. Black bodies (BB) and stellar properties: Top left panel shows the fractional luminosity against the angular size, coloured by the BB’s temperature. Top right panel shows the BB’s temperature against the angular size, coloured by the effective temperature of the star provided by *Gaia*. Bottom panels show the same space coloured by the absolute magnitude M_G (left) and G (right).

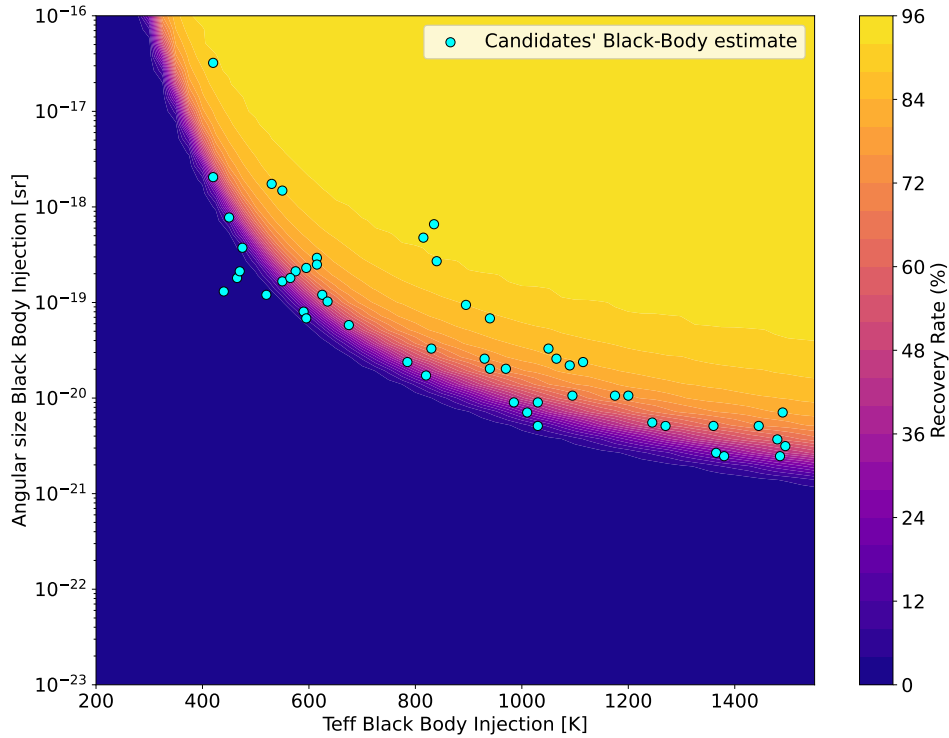


Figure 12. Map of the recovery rate of Black Body injections in a sample of stars similar to our candidates ($\sim 1,500$ stars). Our candidates’ BB estimates are shown as cyan dots.

of outliers to investigate, and we have other methods to validate an excess, to build a rather cheap and efficient approach to the search. The fact that a search for symmetrically similar infrared deficit (see Annex A) led to no candidate or obvious false detection also indicates that this approach is viable in those specific setups.

ACKNOWLEDGMENTS

It is a pleasure to thank Jason Wright, Phil Armitage, and Erwan Allys for valuable discussions.

This work has made use of data from the European Space Agency (ESA) mission *Gaia* (<https://www.cosmos.esa.int/gaia>), processed by the *Gaia* Data Processing and Analysis Consortium (DPAC, <https://www.cosmos.esa.int/web/gaia/dpac/consortium>). Funding for the DPAC has been provided by national institutions, in particular the institutions participating in the *Gaia* Multilateral Agreement.

This publication makes use of data products from the Two Micron All Sky Survey (doi: 10.26131/IRSA2 (Skrutskie et al. 2003)), which is a joint project of the University of Massachusetts and the Infrared Processing and Analysis Center/California Institute of Technology, funded by the National Aeronautics and Space Administration and the National Science Foundation.

This publication makes use of data products from the Wide-field Infrared Survey Explorer, which is a joint

project of the University of California, Los Angeles, and the Jet Propulsion Laboratory/California Institute of Technology, and NEOWISE, which is a project of the Jet Propulsion Laboratory/California Institute of Technology. WISE and NEOWISE are funded by the National Aeronautics and Space Administration.

This publication also makes use of *unWISE* data product (doi:10.26131/IRSA525 (unWISE team 2019; Schlafly et al. 2019)) and *AllWISE* data products (doi: 10.26131/IRSA1 (Wright et al. 2019)).

This research uses services or data provided by the Astro Data Lab at NSF’s National Optical-Infrared Astronomy Research Laboratory. NOIRLab is operated by the Association of Universities for Research in Astronomy (AURA), Inc. under a cooperative agreement with the National Science Foundation.

The Flatiron Institute is a division of the Simons Foundation.

Software: Astropy (Astropy Collaboration et al. 2013, 2018, 2022), numpy (Harris et al. 2020), ARIADNE (Vines & Jenkins 2022), scikit-learn (Pedregosa et al. 2011b), astroquery (Ginsburg et al. 2019), matplotlib (Hunter 2007), pyvo (Graham et al. 2014), scipy (Virtanen et al. 2020), pandas (pandas development team 2020), dustmaps (Green 2018), gaiaxpy (<https://gaia-dpci.github.io/GaiaXPY-website/>, doi: 10.5281/zenodo.8239995).

APPENDIX

A. INFRARED DEFICIT

As a sanity check –and out of curiosity–, we check the results of our pipeline when reversed to look for IR-*deficit* (which, supposedly, cannot happen). By applying a similar methodology (where Eqs 8 and 9 are computed using upper percentiles) we obtain 83 preliminary candidates (*vs* 127 for excess). Applying all the additional cuts (Table 1) on these objects leaves 7 candidates that we plot in Figure 17. Three of those have likely contamination from their environment as shown by the imaging. They do not appear as strong deficit either in *W1* and *W2* according to the SED-fit too. For all of these examples, the *W3* and *W4* land above the SED-fit. However, they also all have a quality flag *U* (meaning that the source measurement had an SNR < 2, and the profile-fit magnitude is a 95% confidence upper limit).

We note also that using the same values used for Eq. 8 and 9 in a symmetric way, i.e. doing the true opposite cut in terms of the “strength” of the anomalies, leads to only 13 deficit candidates in the preliminary cut. All of them then get discarded either by the crowding or the proper-motion disagreement cut.

Thus, we have no IR-deficit candidates that are symmetrically similar in strength to our IR-excess candidates.

REFERENCES

- Arun, R., Mathew, B., Manoj, P., et al. 2019, *AJ*, 157, 159, doi: 10.3847/1538-3881/ab0ca1
- Astropy Collaboration, Robitaille, T. P., Tollerud, E. J., et al. 2013, *A&A*, 558, A33, doi: 10.1051/0004-6361/201322068

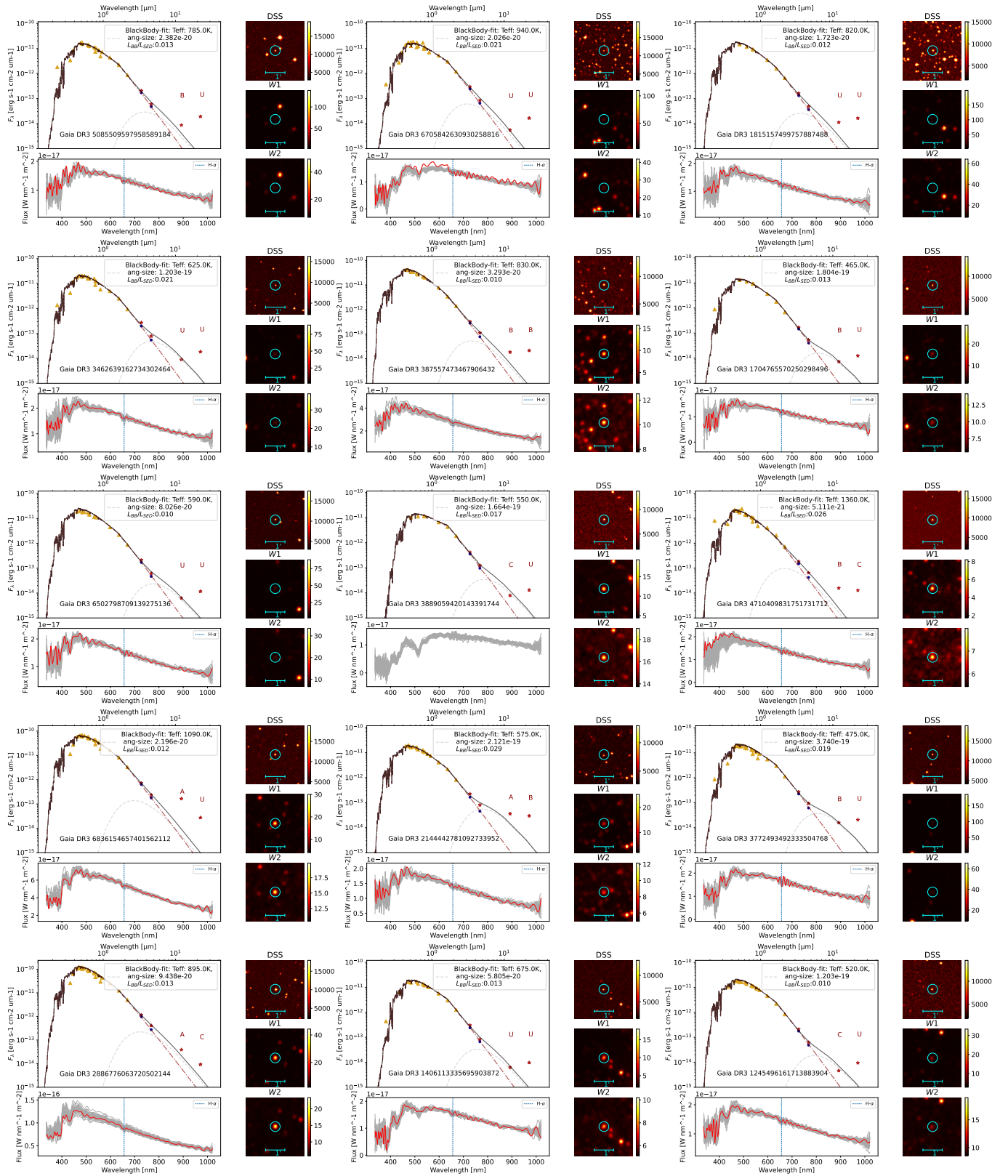


Figure 13. SED and BlackBody fitting for our excess candidates. Yellow triangles are the observations gathered and used by *Ariadne* to compute the SED (dashed dark red line). Red points are the *unWISE* (for *W1* and *W2*) and *AllWISE* (for *W3* and *W4*) values. Blue points are the prediction of our model. The best-fit blackbody is depicted as grey dashed line. The final SED computed as *Ariadne* SED + BlackBody is depicted as a solid black line. Each plot also displays imaging from *AllWISE* (*W1*, *W2*) and *DSS* of a $3'$ square centred on the source candidate. The bottom part of each plot is the *XP* absolute spectra from *Gaia* DR3 computed using *Gaiaxpy* of the object (in red). The spectra of the 30 nearest-neighbors (using *NN-mag*) are in grey. *Ha* line is shown in blue. The letters above *W3* and *W4* are *AllWISE* photometric quality flag.

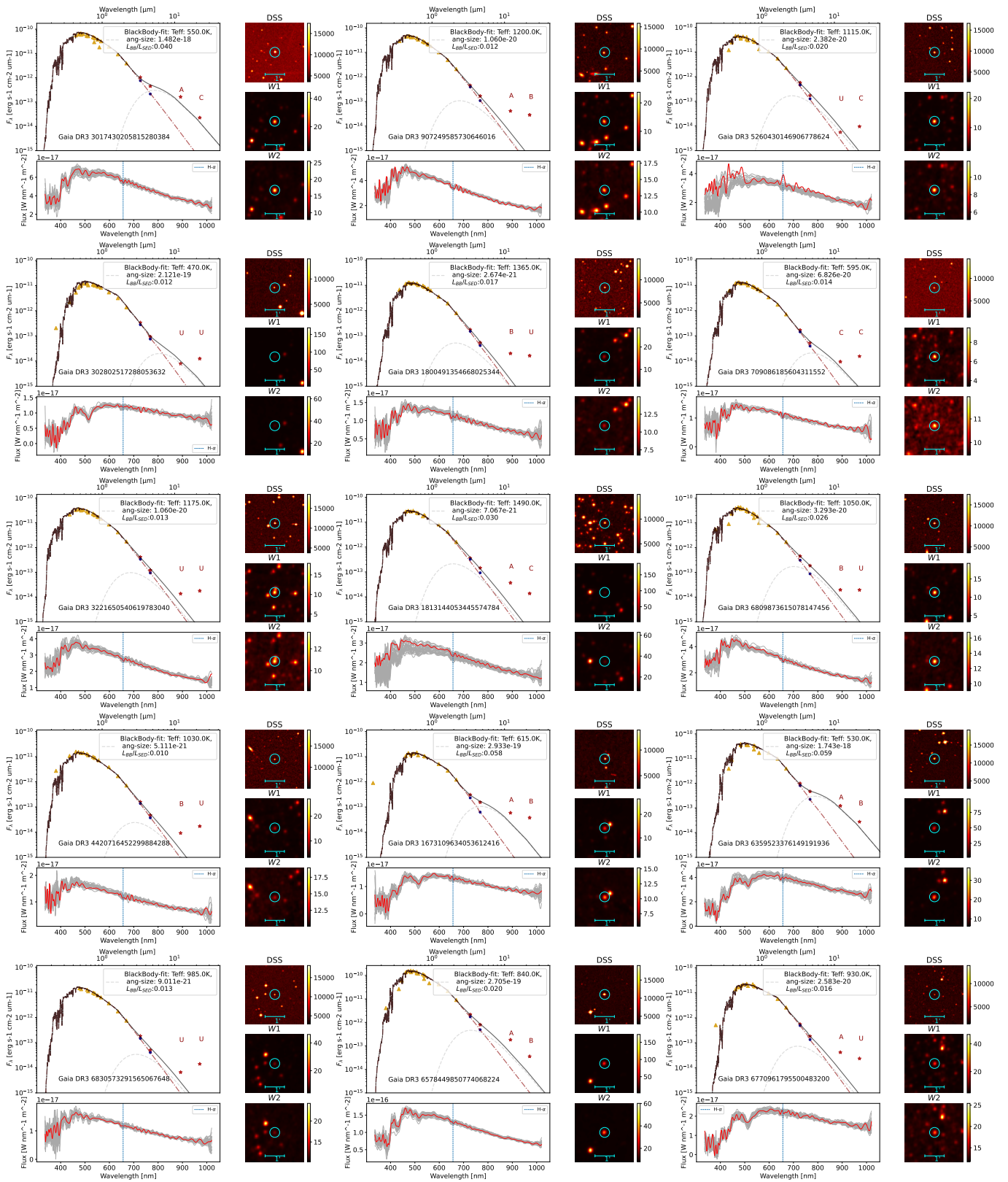


Figure 14. SED and BlackBody fitting for our excess candidates. Yellow triangles are the observations gathered and used by *Ariadne* to compute the SED (dashed dark red line). Red points are the *unWISE* (for *W1* and *W2*) and *AllWISE* (for *W3* and *W4*) values. Blue points are the prediction of our model. The best-fit blackbody is depicted as grey dashed line. The final SED computed as *Ariadne* SED + BlackBody is depicted as a solid black line. Each plot also displays imaging from *AllWISE* (*W1*, *W2*) and *DSS* of a 3' square centred on the source candidate. The bottom part of each plot is the *XP* absolute spectra from *Gaia* DR3 computed using *Gaiaxpy* of the object (in red). The spectra of the 30 nearest-neighbors (using NN-mag) are in grey. *H α* line is shown in blue. The letters above *W3* and *W4* are *AllWISE* photometric quality flag.

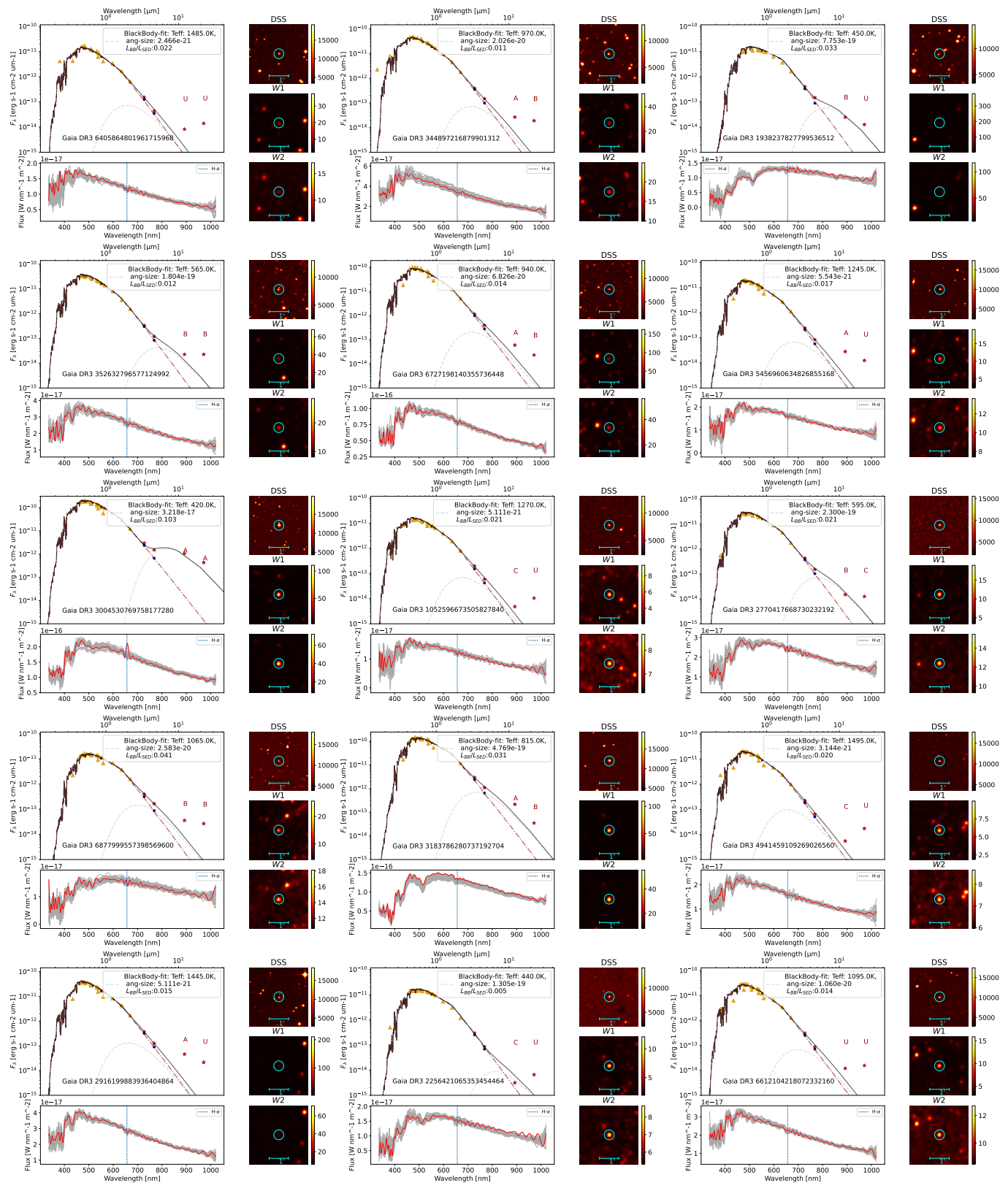


Figure 15. SED and BlackBody fitting for our excess candidates. Yellow triangles are the observations gathered and used by *Ariadne* to compute the SED (dashed dark red line). Red points are the *unWISE* (for *W1* and *W2*) and *AllWISE* (for *W3* and *W4*) values. Blue points are the prediction of our model. The best-fit blackbody is depicted as grey dashed line. The final SED computed as *Ariadne* SED + BlackBody is depicted as a solid black line. Each plot also displays imaging from *AllWISE* (*W1*, *W2*) and *DSS* of a $3'$ square centred on the source candidate. The bottom part of each plot is the *XP* absolute spectra from *Gaia* DR3 computed using *Gaiaxpy* of the object (in red). The spectra of the 30 nearest-neighbors (using NN-mag) are in grey. $H\alpha$ line is shown in blue. The letters above *W3* and *W4* are *AllWISE* photometric quality flag.

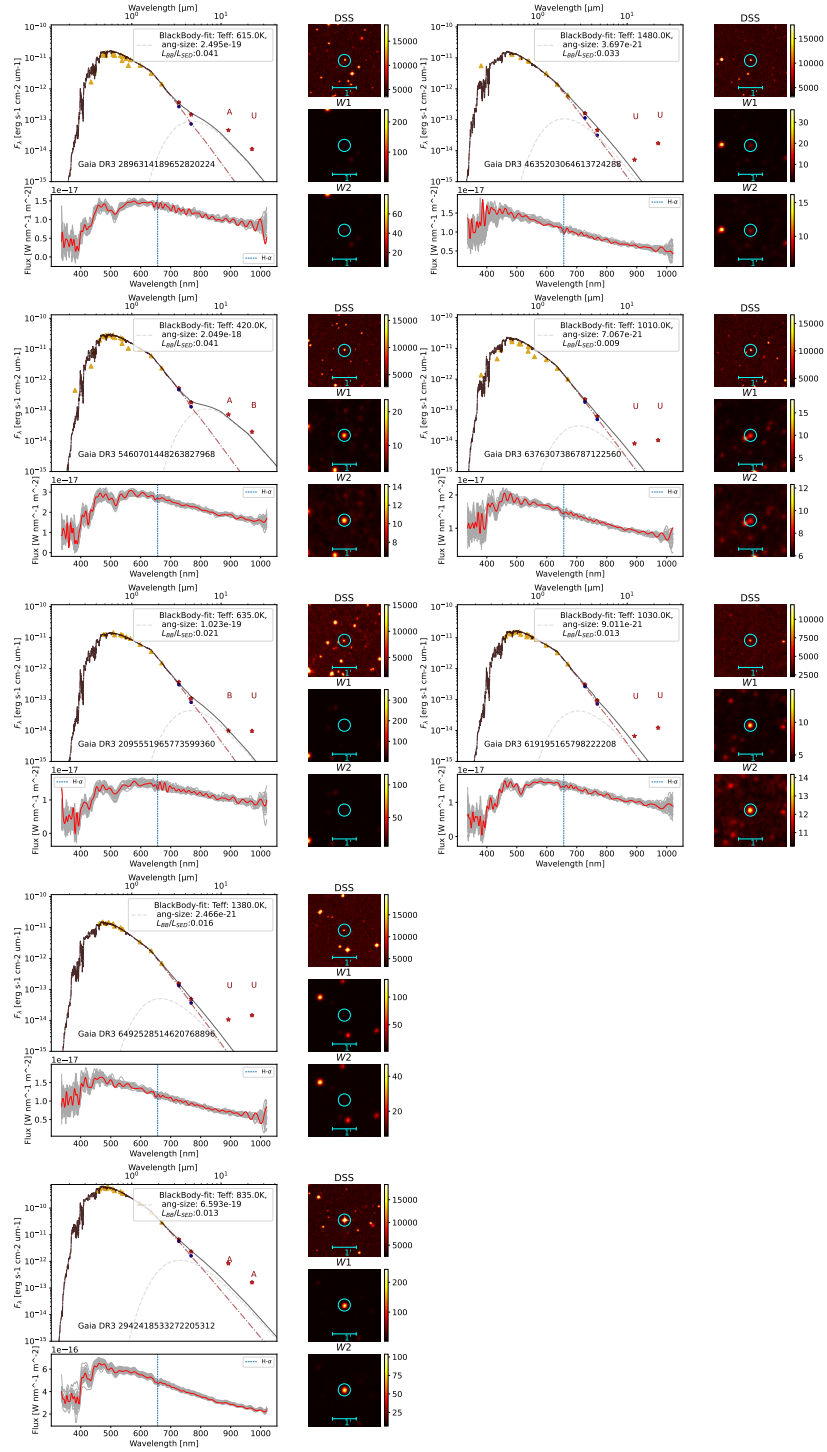


Figure 16. SED and BlackBody fitting for our excess candidates. Yellow triangles are the observations gathered and used by *Ariadne* to compute the SED (dashed dark red line). Red points are the *unWISE* (for *W1* and *W2*) and *AllWISE* (for *W3* and *W4*) values. Blue points are the prediction of our model. The best-fit blackbody is depicted as grey dashed line. The final SED computed as *Ariadne* SED + BlackBody is depicted as a solid black line. Each plot also displays imaging from *AllWISE* *W1*, *W2* and *DSS* of a 3' square centred on the source candidate. The bottom part of each plot is the *XP* absolute spectra from *Gaia* DR3 computed using *Gaiaxy* of the object (in red). The spectra of the 30 nearest-neighbors (using NN-mag) are in grey. $H\alpha$ line is shown in blue. The letters above *W3* and *W4* are *AllWISE* photometric quality flag.

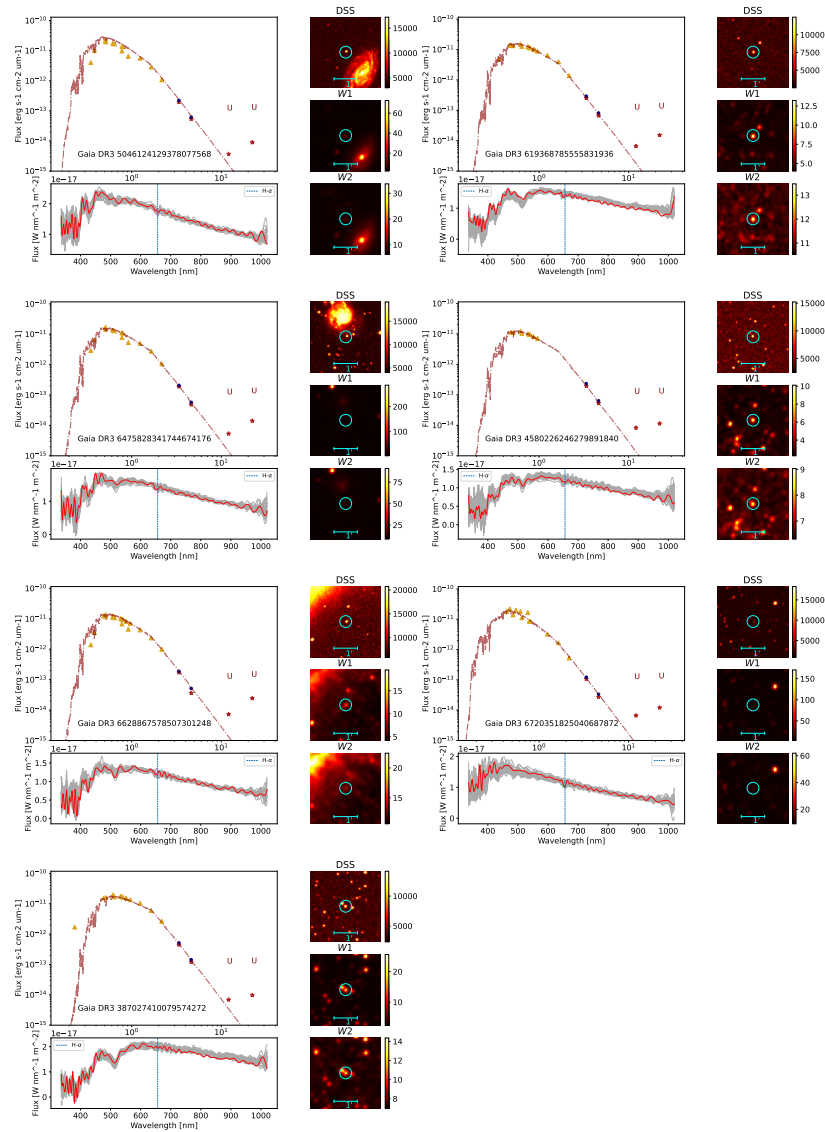


Figure 17. SED, imaging and XP spectra of **IR-deficit candidates**.

Astropy Collaboration, Price-Whelan, A. M., Sipőcz, B. M., et al. 2018, *AJ*, 156, 123, doi: 10.3847/1538-3881/aabc4f

Astropy Collaboration, Price-Whelan, A. M., Lim, P. L., et al. 2022, *ApJ*, 935, 167, doi: 10.3847/1538-4357/ac7c74

Babusiaux, C., Fabricius, C., Khanna, S., et al. 2023, *A&A*, 674, A32, doi: 10.1051/0004-6361/202243790

Ballerini, N. P., Rieke, G. H., Su, K. Y. L., & Montiel, E. 2013, *ApJ*, 775, 55, doi: 10.1088/0004-637X/775/1/55

Balog, Z., Kiss, L. L., Vinkó, J., et al. 2009, *ApJ*, 698, 1989, doi: 10.1088/0004-637X/698/2/1989

Castelli, F., & Kurucz, R. L. 2003, in *Modelling of Stellar Atmospheres*, ed. N. Piskunov, W. W. Weiss, & D. F. Gray, Vol. 210, A20.
<https://arxiv.org/abs/astro-ph/0405087>

Chandola, V., Banerjee, A., & Kumar, V. 2009, *ACM computing surveys (CSUR)*, 41, 1

Cotten, T. H., & Song, I. 2016, *ApJS*, 225, 15, doi: 10.3847/0067-0049/225/1/15

Creevey, O. L., Sordo, R., Pailer, F., et al. 2023, *A&A*, 674, A26, doi: 10.1051/0004-6361/202243688

Cruz-Saenz de Miera, F., Chavez, M., Bertone, E., & Vega, O. 2014, *MNRAS*, 437, 391, doi: 10.1093/mnras/stt1888

Cutri, R. M., Wright, E. L., Conrow, T., et al. 2021, *VizieR Online Data Catalog*, II/328

Da Costa, A. D., Canto Martins, B. L., Leão, I. C., et al. 2017, *ApJ*, 837, 15, doi: 10.3847/1538-4357/837/1/15

Dennihy, E., Farihi, J., Gentile Fusillo, N. P., & Debes, J. H. 2020, *ApJ*, 891, 97, doi: 10.3847/1538-4357/ab7249

Gaia Collaboration, Prusti, T., de Bruijne, J. H. J., et al. 2016, *A&A*, 595, A1, doi: 10.1051/0004-6361/201629272

Gaia Collaboration, Vallenari, A., Brown, A. G. A., et al. 2023, *A&A*, 674, A1, doi: 10.1051/0004-6361/202243940

- Gavras, P., Rimoldini, L., Nienartowicz, K., et al. 2023, *A&A*, 674, A22, doi: 10.1051/0004-6361/202244367
- Ginsburg, A., Sipőcz, B. M., Brasseur, C. E., et al. 2019, *AJ*, 157, 98, doi: 10.3847/1538-3881/aafc33
- Graham, M., Plante, R., Tody, D., & Fitzpatrick, M. 2014, *PyVO: Python access to the Virtual Observatory, Astrophysics Source Code Library*, record ascl:1402.004
- Green, G. 2018, *The Journal of Open Source Software*, 3, 695, doi: 10.21105/joss.00695
- Harris, C. R., Millman, K. J., van der Walt, S. J., et al. 2020, *Nature*, 585, 357, doi: 10.1038/s41586-020-2649-2
- Hidalgo, S. L., Pietrinferni, A., Cassisi, S., et al. 2018, *ApJ*, 856, 125, doi: 10.3847/1538-4357/aab158
- Hunter, J. D. 2007, *Computing in Science & Engineering*, 9, 90, doi: 10.1109/MCSE.2007.55
- Ishida, E. E., Kornilov, M. V., Malanchev, K. L., et al. 2021, *Astronomy & Astrophysics*, 650, A195
- Lochner, M., & Bassett, B. A. 2021, *Astronomy and Computing*, 36, 100481
- Malanchev, K., Kornilov, M. V., Pruzhinskaya, M. V., et al. 2023, *PASP*, 135, 024503, doi: 10.1088/1538-3873/acb292
- Manzo-Martínez, E., Calvet, N., Hernández, J., et al. 2020, *ApJ*, 893, 56, doi: 10.3847/1538-4357/ab7ead
- McDonald, I., Zijlstra, A. A., & Watson, R. A. 2017, *MNRAS*, 471, 770, doi: 10.1093/mnras/stx1433
- Moór, A., Ábrahám, P., Szabó, G., et al. 2021, *ApJ*, 910, 27, doi: 10.3847/1538-4357/abdc26
- Moór, A., Ábrahám, P., Su, K. Y. L., et al. 2024, *MNRAS*, 528, 4528, doi: 10.1093/mnras/stae155
- pandas development team, T. 2020, *pandas-dev/pandas: Pandas, latest*, Zenodo, doi: 10.5281/zenodo.8092754
- Pedregosa, F., Varoquaux, G., Gramfort, A., et al. 2011a, *Journal of Machine Learning Research*, 12, 2825
- . 2011b, *Journal of Machine Learning Research*, 12, 2825
- Rimoldini, L., Holl, B., Gavras, P., et al. 2023, *A&A*, 674, A14, doi: 10.1051/0004-6361/202245591
- Schlafly, E. F., Meisner, A. M., & Green, G. M. 2019, *ApJS*, 240, 30, doi: 10.3847/1538-4365/aafbea
- Schlegel, D. J., Finkbeiner, D. P., & Davis, M. 1998, *ApJ*, 500, 525, doi: 10.1086/305772
- Schmidt, E. G. 2015, *ApJ*, 813, 29, doi: 10.1088/0004-637X/813/1/29
- Sheikh, S. Z. 2020, *International Journal of Astrobiology*, 19, 237, doi: 10.1017/S1473550419000284
- Skrutskie, M. F., Cutri, R. M., Stiening, R., et al. 2003, *2MASS Source Catalog, IRSA*, doi: 10.26131/IRSA2
- Skrutskie, M. F., Cutri, R. M., Stiening, R., et al. 2006, *AJ*, 131, 1163, doi: 10.1086/498708
- Stetson, P. B. 1996, *PASP*, 108, 851, doi: 10.1086/133808
- Suazo, M., Zackrisson, E., Wright, J. T., Korn, A. J., & Huston, M. 2022, *Monthly Notices of the Royal Astronomical Society*, 512, 2988, doi: 10.1093/mnras/stac280
- unWISE team. 2019, *unWISE catalog, IRSA*, doi: 10.26131/IRSA525
- Uzpen, B., Kobulnicky, H. A., Olsen, K. A. G., et al. 2005, *ApJ*, 629, 512, doi: 10.1086/431479
- Vines, J. I., & Jenkins, J. S. 2022, *MNRAS*, doi: 10.1093/mnras/stac956
- Virtanen, P., Gommers, R., Oliphant, T. E., et al. 2020, *Nature Methods*, 17, 261, doi: 10.1038/s41592-019-0686-2
- Wright, E., Eisenhardt, P., Mainzer, A., Ressler, M., & Cutri, R. e. a. 2019, *AllWISE Source Catalog, IRSA1*, doi: 10.26131/IRSA1
- Wyatt, M. C., Panić, O., Kennedy, G. M., & Matrà, L. 2015, *Ap&SS*, 357, 103, doi: 10.1007/s10509-015-2315-6